

Metal-THINGS: The Milky Way twin candidate NGC 3521

L. S. Pilyugin^{1,2}, M. A. Lara-López³, G. Tautvaišienė¹, I. A. Zinchenko^{4,2}, L. E. Garduño⁵, M. E. De Rossi^{6,7},
J. Zaragoza-Cardiel⁸, S. Dib⁹, and G. Valé³

¹ Institute of Theoretical Physics and Astronomy, Vilnius University, Sauletekio av. 3, 10257, Vilnius, Lithuania

² Main Astronomical Observatory, National Academy of Sciences of Ukraine, 27 Akademika Zabolotnoho St, 03680, Kiev, Ukraine

³ Departamento de Física de la Tierra y Astrofísica, Instituto de Física de Partículas y del Cosmos, IPARCOS. Universidad Complutense de Madrid (UCM), E-28040, Madrid, Spain

⁴ Faculty of Physics, Ludwig-Maximilians-Universität, Scheinerstr.1, 81679 Munich, Germany

⁵ Instituto Nacional de Astrofísica, Óptica y Electrónica (INAOE), Luis E. Erro 1, Tonantzintla, Puebla, C.P. 72840, México

⁶ Universidad de Buenos Aires, Facultad de Ciencias Exactas y Naturales y Ciclo Básico Común. Buenos Aires, Argentina

⁷ CONICET-Universidad de Buenos Aires, Instituto de Astronomía y Física del Espacio (IAFE). Buenos Aires, Argentina

⁸ Centro de Estudios de Física del Cosmos de Aragón (CEFCA), Plaza San Juan 1, 44001 Teruel, Spain

⁹ Max Planck Institute for Astronomy, Königstuhl 17, 69117, Heidelberg, Germany

January 14, 2025

ABSTRACT

The 3D spectrophotometry measurements of the galaxy NGC 3521, a structural Milky Way analogue (sMWA), were carried out within the Metal-THINGS project. We found that the oxygen abundance in the inner part of NGC 3521 is at a nearly constant level and the O/H gradient is negative at larger radii. The change in the nitrogen abundance with radius is similar to that for oxygen with the break in the N/H distribution at a smaller radius than the O/H distribution break, but the difference between the break radii is within the uncertainties of these values. The radial distributions of the oxygen abundance, the gas mass fraction, and the effective oxygen yield in NGC 3521 are compared to that of the Milky Way (MW), with the aim of examining the similarity (or disagreement) in their chemical evolutions. The oxygen abundances of two H II regions closest to the centre of the MW (at a radii of 4-5 kpc) are close to the binned oxygen abundances in NGC 3521 at the same galactocentric distances; an accurate value of the central oxygen abundance in the MW cannot be established because of the lack of the measurements near the centre. The oxygen abundances in the outer part of the MW are lower than those in the outer part of NGC 3521. The gas mass fraction in the outer part of the MW is higher than in NGC 3521. The obtained values of the effective oxygen yield, Y_{eff} , in NGC 3521 are close to the empirical estimation of the oxygen yield, Y_O . This suggests that mass exchange with the surroundings plays little to no role in the current chemical evolution of NGC3521. The values of the Y_{eff} in the MW were determined using two variants of the radial distribution of the gas mass surface density. The values of the Y_{eff} in the MW obtained with the first distribution are also close to Y_O , as in NGC 3521. The Y_{eff} in the MW obtained with the second distribution are below Y_O at radii between ~ 6 and ~ 10.4 kpc. This suggests that the mass exchange with the surroundings can play a significant role in the chemical evolution of this part of the MW, in contrast to that in NGC 3521. To draw a solid conclusion about the role of mass exchange with the surroundings in the chemical evolution of the MW it is essential to determine which of these distributions provides a more adequate description of the gas distribution in the MW.

Key words. galaxies: spiral – galaxies: fundamental parameters – galaxies: abundances – ISM: abundances

1. Introduction

The examination of the oxygen abundance distributions in structural Milky Way analogues (sMWAs) is important. Since the oxygen abundance is an indicator of the evolution of a galaxy, the comparison of the oxygen abundance distributions between the Milky Way (MW) and sMWAs, coupled with the comparison of other relevant characteristics (e.g. gas mass fraction), can point out whether the chemical evolution of the MW is similar to (or differs from) the chemical evolutions of the sMWAs. This can clarify whether the MW is really a typical spiral galaxy, and in what ways it differs from typical spiral galaxies if this is not the case. This is important for the theory of formation and evolution of galaxies. The search for Milky Way-like galaxies has been the subject of many investigations (e.g. de Vaucouleurs & Pence 1978; Hammer et al. 2007; Mutch et al. 2011; Licquia et al. 2015, 2016; McGaugh 2016; Fraser-McKelvie et al. 2019; Boardman et al. 2020a; Fielder et al. 2021; Pilyugin & Tautvaišienė 2024). It was noted

by Boardman et al. (2020a) that there is no single and commonly accepted definition of a Milky Way-like galaxy; rather, the definition can change depending on the goals of a particular study. Different characteristics of the MW (morphological type T , isophotal diameter, effective diameter, absolute B magnitude, mean colour index ($B - V$), presence of spiral arms, presence of a bar, stellar mass, bulge-to-total ratio, rotation velocity) have been used when comparing the MW to other galaxies. Galaxies may be identified as being Milky Way-like on the basis of having similar qualitative characteristics to the MW or on the basis of their position relative to the MW in a given parameter space. The selection of Milky Way-like galaxies using only two characteristics of the MW as the selection criteria is based on the Copernican assumption that the MW is not extraordinary amongst galaxies; that is, any property of the MW is similar to that of the Milky Way-like galaxies selected (Mutch et al. 2011; Licquia et al. 2015; Boardman et al. 2020a).

It was suggested to distinguish between structural Milky Way analogues and evolutionary Milky Way analogues (Pilyugin & Tautvaišienė 2024). The characteristics of a galaxy can be conditionally divided into two types. The parameters of the first type (e.g. morphology, luminosity, stellar mass, rotation velocity) describe the structure and global characteristics of a galaxy at the present-day epoch, and can be called structural parameters. The parameters of the second type are related to the evolution of a galaxy. The oxygen abundance at a given radius of a galaxy is defined by the evolution of this region (fraction of gas converted into stars, i.e. astration level, and matter exchange with the surroundings). Thus, the oxygen abundance can be considered as an indicator of a galaxy's evolution and can be called an evolutionary parameter. A galaxy located close to the MW in the field(s) of the first type of parameters should be referred to as a structural Milky Way analogue (sMWA). A galaxy located close to the MW in the field of the second type of parameters should be referred to as an evolutionary Milky Way analogue (eMWA). If a galaxy is simultaneously an sMWA and an eMWA, then such galaxy should be considered a Milky Way twin.

sMWAs were selected and examined in the papers cited above. It was found that the galaxy NGC 3521 has structural parameters (stellar mass, rotation velocity, optical radius) that are very similar to those of the MW; these quantities are identical within the uncertainties, which means that NGC 3521 is a near structural analogue to the MW (McGaugh 2016). It is interesting to note that the mass of the supermassive black hole at the centre of the Milky Way, $M_{BH} = 4.15 \pm 0.01 \times 10^6 M_{\odot}$ or $\log(M_{BH}/M_{\odot}) = 6.618$, derived using the star orbit around the black hole (Gravity Collaboration 2019) is also close to the supermassive black hole mass in NGC 3521, $\log(M_{BH}/M_{\odot}) = 6.85 \pm 0.58$, estimated using an established relationship between the logarithmic spiral arm pitch angle and the mass of the central supermassive black hole in their host galaxies (Davis et al. 2014).

The spectra of ten H II regions in NGC 3521 were measured by Zaritsky et al. (1994), three H II regions by Bresolin et al. (1999), and one H II region by López et al. (2019). A mandatory requirement for comparing the oxygen abundances in the MW and NGC 3521 is that the abundances must be determined using the same metallicity scale. The oxygen abundances in the H II regions of the MW are determined through the direct T_e method. Therefore, we used the R calibration from Pilyugin & Grebel (2016) in the determinations of the oxygen abundances in H II regions of NGC 3521 since the R calibration provides abundances compatible with the metallicity scale defined by the T_e -based abundances. Unfortunately, Zaritsky et al. (1994) did not measure the fluxes of the nitrogen emission line $[\text{N II}]\lambda 6584$ required for the abundance determination through the R calibration. Thus, the R calibration-based abundances can be estimated only in the H II regions of NGC 3521 measured by Bresolin et al. (1999) and López et al. (2019). Grasha et al. (2022) identified 92 H II regions in NGC 3521 using data from the TYPHOON programme, an integral field spectroscopic survey of 44 nearby, large angular-size galaxies observed with the 2.5 m du Pont Telescope at the Las Campanas Observatory, Chile. Grasha et al. (2022) measured the emission-line fluxes of the H II regions and determined their oxygen abundances using the N2O2 calibration from Kewley & Dopita (2002). They measured the radial oxygen abundance gradient across NGC 3521. However, the values they used for the geometric parameters (e.g. the optical radius and the position angle of the major axis) of NGC 3521 are inaccurate. Their adopted value of the optical radius R_{25} is less than a half of that reported in the RC3 catalogue (de Vaucouleurs et al.

1991). Their adopted value of the position angle of the major axis is $\text{PA}=107^\circ$, while PA is $\sim 163^\circ$, north-eastwards, in RC3 and other catalogues. The value of $\text{PA} \sim 341^\circ$ (or $\text{PA} \sim 161^\circ$, north-eastwards) was derived from the analysis of the velocity fields of the ionised hydrogen, neutral hydrogen, and CO (2–1) emission (Daigle et al. 2006; de Blok et al. 2008; Lang et al. 2020). Taking into account that NGC 3521 is a galaxy with a high inclination, the use of the correct value of the position angle of the major axis is crucial in the determinations of the galactocentric distances of H II regions. Therefore, the value of the oxygen abundance gradient obtained in Grasha et al. (2022) is unreliable. This hinders the ability to determine the similarities or discrepancies in the evolutionary paths of NGC 3521 and the MW, making it difficult to conclude whether NGC 3521 is a true evolutionary analogue of the Milky Way.

Three pointings of NGC 3521 were observed with integral field spectroscopy as part of the Metal-THINGS survey (Lara-López et al. 2021, 2023). The blue and red spectra were observed, and the emission lines necessary for abundance determinations through the R calibration from Pilyugin & Grebel (2016) were measured. This allowed the derivation of the radial abundance distribution across NGC 3521 on a metallicity scale that is compatible with the T_e -based oxygen abundances in the MW. By comparing the radial distributions of the oxygen abundances, gas mass fractions, and effective oxygen yields in NGC 3521 and the MW, we can identify similarities or discrepancies in their chemical evolutions. This is the goal of the current study.

This paper is organised in the following way. The observations and data reduction of NGC 3521 are described in Sect. 2. In Sect. 3 the determinations of the orientation of NGC 3521 in space, the rotation curve, and the radial abundance distribution are reported. The comparison between NGC 3521 and the Milky Way is given in Sect. 4, and Sect. 5 provides a brief summary.

2. Observations and data reduction

The observations of NGC 3521 were carried out as part of the Metal-THINGS survey using the 2.7 m Harlan Schmidt telescope, McDonald Observatory, Texas, in March 2022. The Integral Field Unit (IFU) George and Cynthia Mitchell Spectrograph (GCMS, Hill et al. 2008) was used in the blue and red setup with the low-resolution grating VP1 with a resolution of 5.3 \AA . The average seeing during the observations was 1.7 arcsec , and a total of three pointings were observed, as shown in Fig. 1.

The GCMS is a square array of $100 \times 102 \text{ arcsec}$, with a spatial sampling of 4.2 arcsec , and a 0.3 filling factor. Every pointing is observed with three dither positions to ensure a 90% surface coverage. The IFU consists of 246 fibres arranged in a fixed pattern. Each fibre has a 4.2 arcsec diameter, and hence that is the approximate spatial resolution. At the adopted distance of 10.7 Mpc to this galaxy (see below), the 4.2 arcsec fibre corresponds to 217.3 parsec . Due to the extended nature of this galaxy, off-source sky exposures were taken for sky subtraction during the data reduction process. Every pointing was observed for 900 seconds per dither, followed by a sky exposure, and the same process was repeated until a total of 45 minutes per dither was reached.

The data reduction was performed as described in Lara-López et al. (2021, 2023). The basic data reduction (bias subtraction, flat frame correction, and wavelength calibration) was performed using P3D.¹ The rest of the data reduction, including sky subtraction, flux calibration, combination of dithers,

¹ <https://p3d.sourceforge.io>

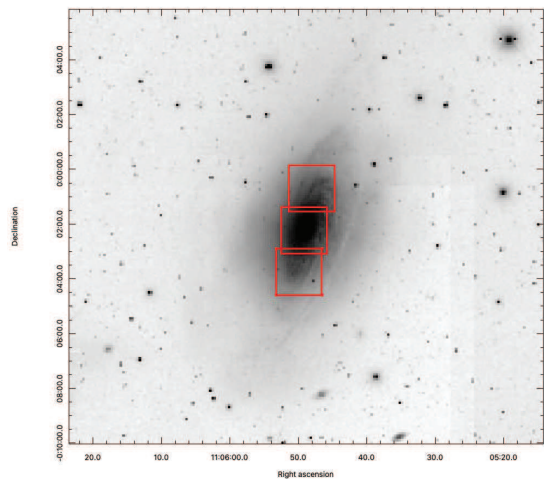


Fig. 1. Observed GCMS pointings superimposed on a NGC 3521 image from the Cerro Tololo Inter-American Observatory (CTIO), 1.5m telescope.

and mosaic generation, was performed using our own routines in Python. Since we used several individual pointings for the same galaxy, astrometry was applied to each pointing. First, each pointing was converted into a collapsed data cube; then we identified several stars and used the same star positions from the Two Micron All-Sky Survey (2MASS, Skrutskie et al. 2006). Next we applied the astrometry to each pointing using our own routines in Python (for more details, see Garduño et al. 2023). Finally, we assembled all the individual pointings and built a mosaic for this galaxy.

The stellar continuum of all flux-calibrated spectra was fitted using STARLIGHT (Cid Fernandes et al. 2005; Asari et al. 2007; for a detailed description of this procedure, see Zinchenko et al. 2016). In summary, to fit the continuum 45 simple stellar population (SSP) models from the evolutionary synthesis models of Bruzual & Charlot (2003) were used, with ages from 1 Myr up to 13 Gyr and metallicities $Z = 0:005, 0.02,$ and 0.05 . The fitted continuum was subtracted from the spectra, and the emission lines were measured using Gaussian line-profile fittings. In this paper the individual spectra of the fibres are used, which are independent of each other. This is in contrast to other IFU data that rely on image spaxels.

3. Determination of the properties of NGC 3521

3.1. Orientation in the space and rotation curve

The geometrical parameters of the galaxy (such as the coordinates of its centre, the position angle of the major axis, the inclination angle, and the isophotal radius) are necessary for determining the galactocentric distances of individual fibres and constructing radial distributions of various characteristics. The orientation of the galaxy in space can be derived by the best fit to the observed line-of-sight velocity field. The measured wavelength of the observed $H\alpha$ emission line provides the line-of-sight velocity of each region (fibre), denoted as $V_{H\alpha}$. The observed line-of-sight velocities, V_{los} , are recorded on a set of fibre coordinates RA and DEC. Panel (a) of Fig. 2 shows the line-of-sight velocity V_{los} field across the image of NGC 3521 in sky coordinates (arcsec) where the measured $V_{H\alpha}$ velocity is corrected for the obtained velocity of the centre of the galaxy with respect to the Sun, the systemic velocity V_{sys} , that is $V_{los} = V_{H\alpha} - V_{sys}$.

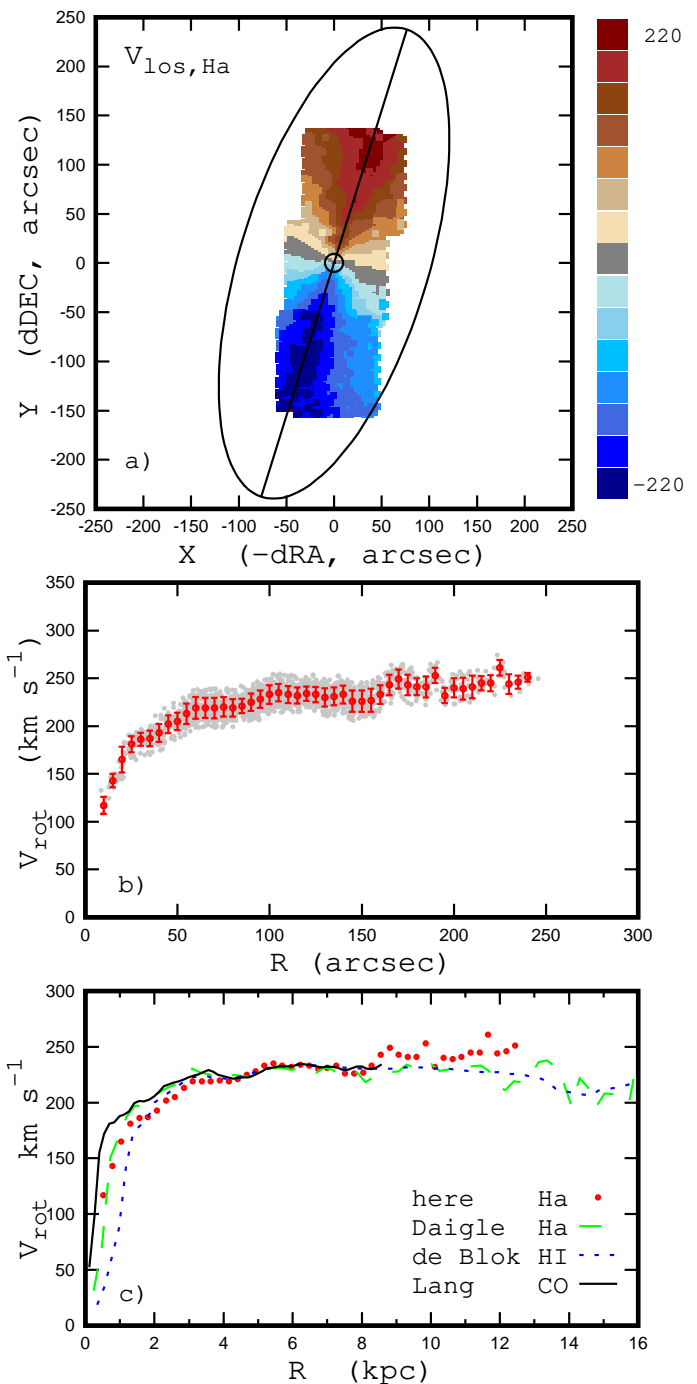


Fig. 2. Rotation curve of NGC 3521. *Panel a:* Line-of-sight $H\alpha$ velocity (km s^{-1}) field in sky coordinates (arcsec). The values of the V_{los} are colour-coded. The circle shows the kinematic centre of the galaxy; the line indicates the position of the major kinematic axis of the galaxy; the ellipse is the optical radius. *Panel b:* Rotation curve of NGC 3521. The grey points mark the individual fibres used in the determination of the final rotation curve. The red circles denote the mean values of the rotation velocity in bins of 5 arcsec in the radius, and the bars show the scatter in rotation velocities about the mean value in the bins. *Panel c:* Comparison of the obtained rotation curve with those from the literature. The red points show the rotation curve obtained here from the $H\alpha$ velocity field; the green dashed line denotes the rotation curve determined by Daigle et al. (2006) from the $H\alpha$ velocity field; the blue dotted line marks the rotation curve derived by de Blok et al. (2008) from the HI velocity field; and the dark solid line is the rotation curve derived by Lang et al. (2020) from the CO velocity field.

The determination of the galaxy’s geometrical parameters and the rotation curve from the observed velocity field is performed using standard method (e.g. Warner et al. 1973; Begeman 1989; de Blok et al. 2008; Oh et al. 2018). The parameters that define the observed velocity field of a galaxy with a symmetrically rotating disc are as follows:

- the coordinates of the galaxy’s rotation centre, RA_{centre} and DEC_{centre} ;
- the velocity of the galaxy’s centre relative to the Sun, the systemic velocity V_{sys} ;
- the circular velocity V_{rot} at the distance R from the galaxy’s centre;
- the position angle PA of the major kinematic axis;
- the kinematic inclination angle i , which is the angle between the normal to the plane of the galaxy rotation and the line of sight.

The parameters RA_{centre} , DEC_{centre} , V_{sys} , PA , i , and the rotation curve $V_{rot}(R)$ are derived by the best fit to the observed velocity field $V_{los}(RA, DEC)$. We used the iterative procedure discussed in Pilyugin et al. (2019). In brief, in the first step the values of RA_{centre} , DEC_{centre} , PA , i , and the rotation curve are determined using all the available line-of-sight velocity measurements. At each step, data points with large deviations (larger than 21 km s^{-1} , which is 3σ for differences between the measured $H\beta$ and $H\alpha$ velocities; Pilyugin et al. 2019) from the rotation curve obtained in the previous step are rejected, and new values of the parameters and of the rotation curve $V_{rot}(R)$ are derived. The iteration is stopped when the absolute value of the difference of RA_{centre} (and DEC_{centre}) obtained in successive steps is less than $0''.1$, the difference of PA (and i) is smaller than 0.1° , and the rotation curves agree within 1 km/s (at each radius).

The following values of the geometrical parameters were derived: $RA_{centre} = 166^\circ 45' 17.52''$, $DEC_{centre} = -0^\circ 03' 59.79''$, $V_{sys} = 709.1 \text{ km/s}$, $PA = 342.2^\circ$, and $i = 66.7^\circ$. The obtained position of the rotation centre of the galaxy and the position angle of the major kinematic axis are shown in panel (a) of Fig. 2. The derived rotation curve of NGC 3521 is shown in panel (b) of Fig. 2. The geometrical angles and the rotation curve derived from the stellar line-of-sight velocity field are close to those derived from the line-of-sight velocity field of the ionised gas.

We now compare the geometrical angles of NGC 3521 obtained here with those from the literature. Daigle et al. (2006) measured the $H\alpha$ line-of-sight velocity field in NGC 3521 based on Fabry–Perot observations. From their analysis of the observed $H\alpha$ velocity field, they derived the kinematical angles and the rotation, finding $PA = 342.0 \pm 1.1^\circ$ and an inclination angle of $i = 66.7 \pm 2.0^\circ$.

NGC 3521 was also studied as part of The HI Nearby Galaxy Survey (THINGS) project, a high spectral ($\lesssim 5.2 \text{ km/s}$) and spatial ($\sim 6''$) resolution survey of HI 21 cm emission in 34 nearby galaxies obtained using the NRAO Very Large Array (VLA) (Walter et al. 2008). Using the velocity field of the HI emission line, de Blok et al. (2008) determined the position angle of the major kinematic axis, the inclination angle, and the rotation curve for NGC 3521, reporting $PA = 339.8^\circ$ and $i = 72.7^\circ$. NGC 3521 is also part of the sample of galaxies of the Physics at High Angular resolution in Nearby Galaxies (PHANGS)–Atacama Large Millimeter/submillimeter Array (ALMA) project (PHANGS–ALMA; Leroy et al. 2021). The CO (2–1) emission in this sample of galaxies is mapped at high ($\sim 1''$) angular resolution. Using the CO data from PHANGS–ALMA, Lang et al. (2020) derived the kinematical angles and rotation curve for NGC 3521, finding $PA = 343.0^\circ$ and $i = 68.8^\circ$.

Thus, the geometrical angles obtained in this study are in excellent agreement with those of Daigle et al. (2006) for the velocity field of ionised hydrogen. The differences in the angles based on the velocity fields of ionised hydrogen and molecular gas are within $\sim 2^\circ$, while the difference in inclination angle between the ionised and atomic gas measurements is approximately $\sim 6^\circ$. The geometrical angles obtained here are used to determine the galactocentric distances of individual fibres.

Different distances to NGC 3521 have been adopted in different studies: $d = 9 \text{ Mpc}$ in Daigle et al. (2006), $d = 10.7 \text{ Mpc}$ in de Blok et al. (2008), $d = 11.2 \text{ Mpc}$ in Lang et al. (2020). We adopted the intermediate value, the distance of $d = 10.7 \text{ Mpc}$ used in the THINGS project. We also adopted an optical radius for NGC 3521 of $R_{25} = 4.16 \text{ arcmin}$ or 249.6 arcsec from the HyperLeda² database (Makarov et al. 2014). At this adopted distance the physical optical radius of NGC 3521 is $R_{25} = 12.94 \text{ kpc}$. The chosen values of the distance and optical (isophotal) radius are used to convert the galactocentric distances of individual fibres from arcsec to galactocentric distances in a physical scale (kpc), and to the fractional galactocentric distances (normalised to the optical radius) in the galaxy plane.

In panel (c) of Fig. 2 we compare the rotation curve obtained here using the $H\alpha$ velocity field with those from previous studies determined using the $H\alpha$ velocity field (Daigle et al. 2006), the HI velocity field (de Blok et al. 2008), and the CO velocity field (Lang et al. 2020). Panel (c) of Fig. 2 reveals a significant discrepancy between the rotation curves derived from different velocity indicators in the central region of the galaxy ($\lesssim 2 \text{ kpc}$), while the two curves based on $H\alpha$ velocity fields are relatively close to each other. Our rotation curve shows satisfactory agreement with the others in the range $3 \text{ kpc} \lesssim R \lesssim 8.5 \text{ kpc}$, though it is slightly higher at larger radii. The discrepancy at large radii may be due to the fact that our measurements along the galaxy’s major axis cover only $\sim 8.5 \text{ kpc}$ (see panel (a) of Fig. 2). Data points near the major axis provide the most reliable information for the determination of the rotation curve.

3.2. Radial abundance distribution

The precision of the line flux measurements is specified by the ratio of the flux error to the flux, ε . We selected a sample of fibre spectra for which the parameter ε is less than the adopted limit value for each line necessary for the abundance determination using the R calibration from Pilyugin & Grebel (2016). The necessary emission lines include the oxygen doublet $[O \text{ II}]\lambda 3727, \lambda 3729$, the $H\beta$ line, the oxygen line $[O \text{ III}]\lambda 5007$, the $H\alpha$ line, and the nitrogen line $[N \text{ II}]\lambda 6584$. The oxygen doublet $[O \text{ II}]\lambda 3727, \lambda 3729$ is from the blue spectrum, while the remaining lines are from the red spectrum. To ensure consistency between the line fluxes in the blue and red spectra, we also required that the absolute value of the relative discrepancy between the $H\beta$ fluxes in the red and blue spectra $(H\beta_{blue} - H\beta_{red}) / (0.5(H\beta_{blue} + H\beta_{red}))$ is smaller than the adopted ε value.

Since the $[O \text{ III}]\lambda 5007$ and $\lambda 4959$ lines originate from transitions at the same energy level, their flux ratio is governed only by the transition probability ratio, which is close to 3 (Storey & Zeippen 2000). Therefore, the value of R_3 can be well approximated as $R_3 = 1.33 \times I_{[O \text{ III}]\lambda 5007} / I_{H\beta}$. Given that the stronger $[O \text{ III}]\lambda 5007$ line is usually measured with higher precision than the weaker $[O \text{ III}]\lambda 4959$ line, we estimated the value of R_3 in that way, and not as the sum of the line fluxes $R_3 = I_{[O \text{ III}]\lambda 4959 + \lambda 5007} / I_{H\beta}$. Similarly, the $[N \text{ II}]\lambda 6584$ and $\lambda 6548$

² <http://leda.univ-lyon1.fr/>

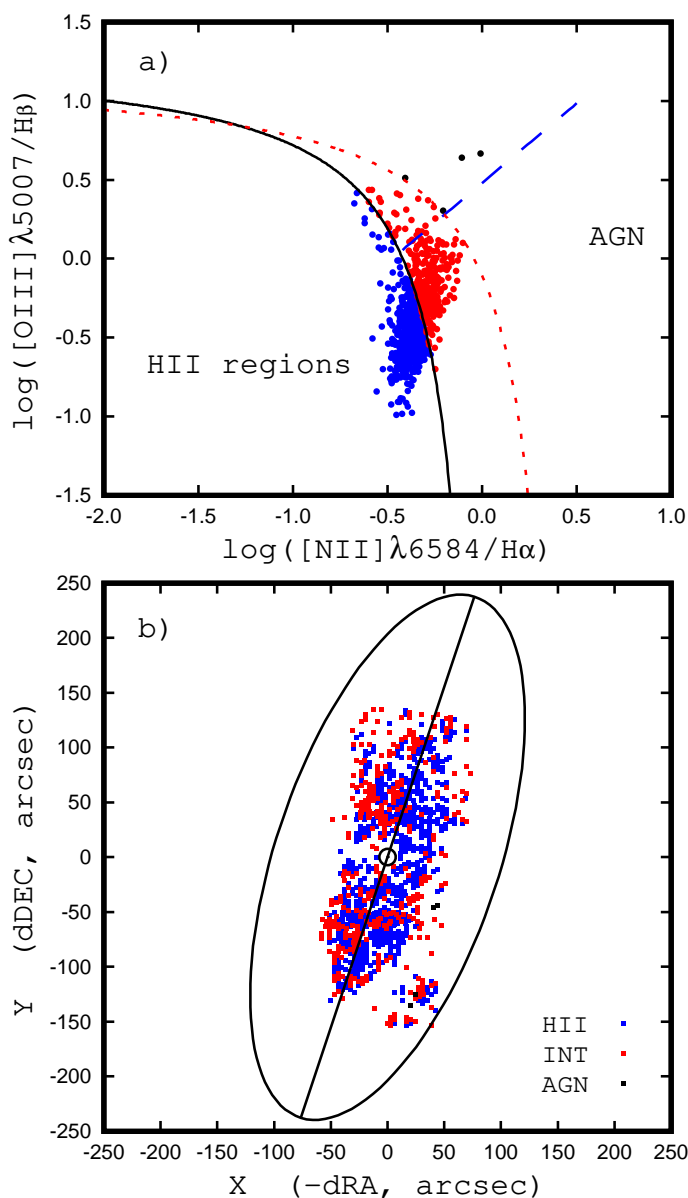


Fig. 3. BPT types of the fibre spectra in NGC 3521. *Panel a:* BPT diagram for the individual fibres in NGC 3521. The blue symbols denote the fibres with H II-region-like spectra, the red symbols mark the fibres with intermediate BPT-type spectra, and the black symbols are the fibres with AGN-like spectra. The solid and short-dashed curves mark the demarcation lines between AGNs and H II regions defined by Kauffmann et al. (2003) and Kewley et al. (2001), respectively. The long-dashed line is the dividing line between Seyfert galaxies and LINERs defined by Cid Fernandes et al. (2010). *Panel b:* Distribution of the fibres with different BPT-type spectra across the image of NGC 3521. The BPT types of spectra are colour-coded as in panel (a). The circle shows the kinematic centre of the galaxy, the line indicates the position of the major kinematic axis of the galaxy, and the ellipse corresponds to the optical radius of the galaxy.

lines also originate from transitions at the same energy level, and the transition probability ratio for those lines is again close to 3 (Storey & Zeippen 2000). Consequently, we also estimated the value of N_2 as $N_2 = 1.33 \times I_{[\text{N II}]\lambda 6584}/I_{\text{H}\beta}$.

We initially adopted a limit value of $\varepsilon = 0.3$, which is satisfied by the required emission lines in the spectra of 926 fibres out of 2214 fibres. The measured line fluxes in the spectra are corrected for interstellar reddening using the reddening law of

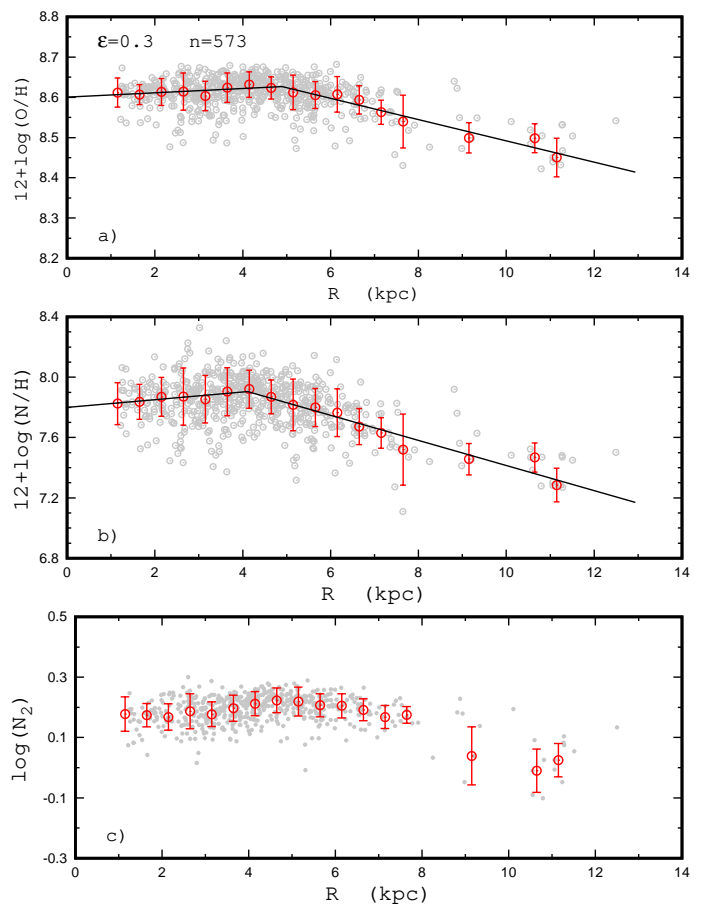


Fig. 4. Abundance properties of NGC 3521 traced by the fibres where the line flux errors $\varepsilon < 0.3$. *Panel a:* Radial oxygen abundance distribution. The grey circles denote the R calibration-based abundances for the individual fibres. The red circles denote the median values of the oxygen abundances in bins of 0.5 kpc in radius, and the bars show the scatter in O/H around the median value of each bin. The line shows the $\text{O}/\text{H} - R$ relation for those data. *Panel b:* Same as panel (a), but for the nitrogen abundances. *Panel c:* Intensity of the emission nitrogen line N_2 as a function of radius. The notations are as in panel (a).

Cardelli et al. (1989) with $R_V = 3.1$. The logarithmic extinction at $\text{H}\beta$ is estimated through a comparison between the measured and theoretical $F_{\text{H}\alpha}/F_{\text{H}\beta}$ ratios where the theoretical value of the line ratio ($= 2.87$) is taken from Osterbrock & Ferland (2006), assuming the case B recombination. If the measured value of the $F_{\text{H}\alpha}/F_{\text{H}\beta}$ ratio is lower than the theoretical value, then a reddening value of zero is adopted.

We classified the excitation of each spectrum using its position on the standard diagnostic Baldwin-Phillips-Terlevich (BPT) diagram $[\text{N II}]\lambda 6584/\text{H}\alpha$ versus the $[\text{O III}]\lambda 5007/\text{H}\beta$, suggested by Baldwin et al. (1981). As in our previous studies (Zinchenko et al. 2019; Pilyugin et al. 2020, 2021), the spectra located to the left of (below) the demarcation line of Kauffmann et al. (2003) are referred to as SF-like or H II region-like spectra (blue symbols in panel (a) of Fig. 3); those located to the right of (above) the demarcation line of Kewley et al. (2001) are referred to as active galactic nucleus (AGN)-like spectra (dark symbols in panel (a) of Fig. 3); and the spectra located between the two demarcation lines are classified as intermediate (INT) spectra (red symbols in panel (a) of Fig. 3). Panel (b) of Fig. 3 shows the distribution of the individual fibres of different BPT types across the image of NGC 3521.

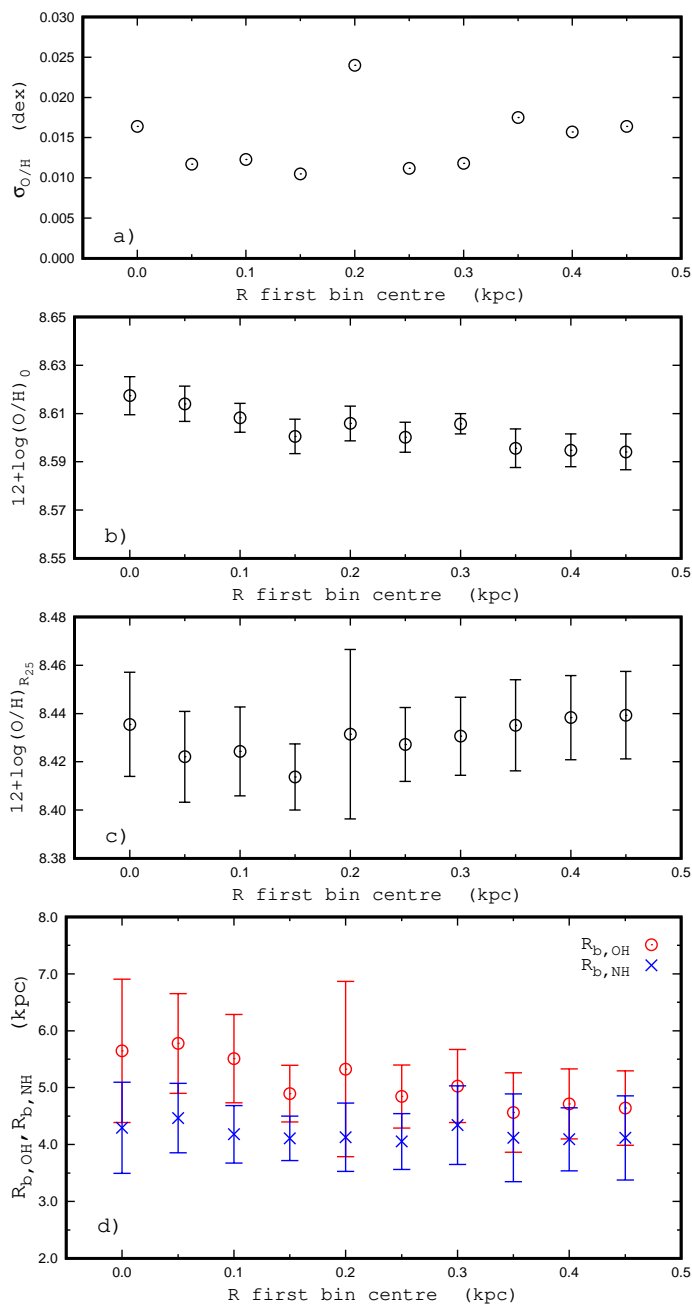


Fig. 5. Dependence of the parameters of the derived oxygen abundance distribution in NGC 3521 on the positions of the centres of bins. *Panel a:* Mean value of the deviations of the binned oxygen abundance around the obtained broken $O/H - R$ relation as a function of the position of the centre of the first bin. *Panel b:* Derived value of the central oxygen abundance as a function of the position of the first bin centre. The bars show the uncertainties of the obtained values. *Panel c:* Same as panel (b), but for the abundances at the isophotal radius. *Panel d:* Value of the break radius as a function of the position of the centre of the first bin. The circles denote the break radius in $O/H - R$ distribution, and the crosses mark the break radius in $N/H - R$ distributions. The bars show the uncertainties of the obtained values.

The oxygen and nitrogen abundances can be determined for fibres with the H II region-like spectra using the R calibration from Pilyugin & Grebel (2016). In our previous paper (Pilyugin et al. 2022), we tested the applicability of R calibration to the IFU spectra. We estimated the calibration-based abundances obtained using both the IFU and the slit spectroscopy for

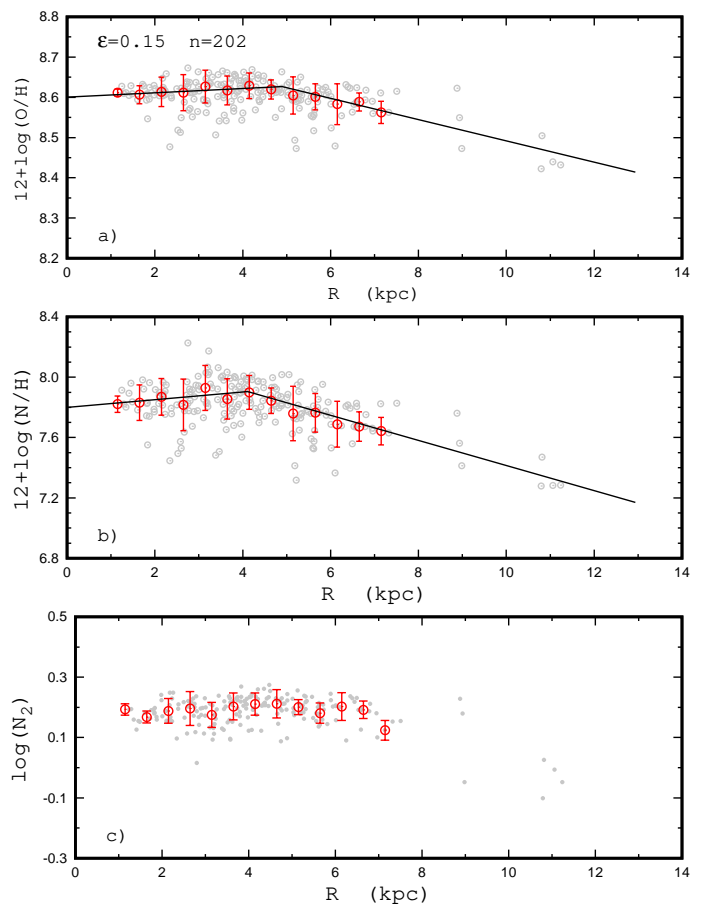


Fig. 6. Abundance properties of NGC 3521 traced by the fibres where the line flux errors $\varepsilon < 0.15$. *Panel a:* Radial oxygen abundance distribution. The grey circles denote the R calibration-based abundances for the individual fibres. The red circles denote the median values of the oxygen abundances in bins of 0.5 kpc in radius, and the bars show the scatter in O/H around the median value of each bin. The line shows the $O/H - R$ relation for the case of $\varepsilon < 0.30$ (from panel (a) of Fig. 4). *Panel b:* Same as panel (a), but for the nitrogen abundances. *Panel c:* Intensity of the emission nitrogen line N_2 as a function of radius. The notations are as in panel (a).

eight nearby galaxies. We find that the IFU and the slit spectra-based abundances obtained through the R calibration are close to each other; the mean value of the differences of binned abundances is within 0.01 dex. We also found that the R calibration can produce close estimations of the abundances using IFU spectra obtained with different spatial resolutions and different spatial samplings.

While the BPT diagram is a commonly used tool to identify the ionising source of nebular emission, the reliability of classifying the ionising source using only the BPT diagram has been questioned (Cid Fernandes et al. 2010, 2011; Sánchez et al. 2014, 2021, 2024; Lacerda et al. 2018; D’Agostino et al. 2019; Johnston et al. 2023). It has been suggested to use the equivalent width of the $H\alpha$ emission line or the gas velocity dispersion as a diagnostic indicator in addition to the emission-line ratios that form the basis of the BPT diagnostic diagram. It has been argued (e.g. Sánchez et al. 2024) that the ionisation in objects with a $EW_{H\alpha} < 6 \text{ \AA}$ is due to hot, old, low-mass, evolved stars (post-AGBs), which are associated with retired regions in galaxies where no star formation occurs. Thus, fibres classified as H II region-like spectra based on the BPT diagram but with $EW_{H\alpha} < 6 \text{ \AA}$ are excluded from the abundance determinations. It should

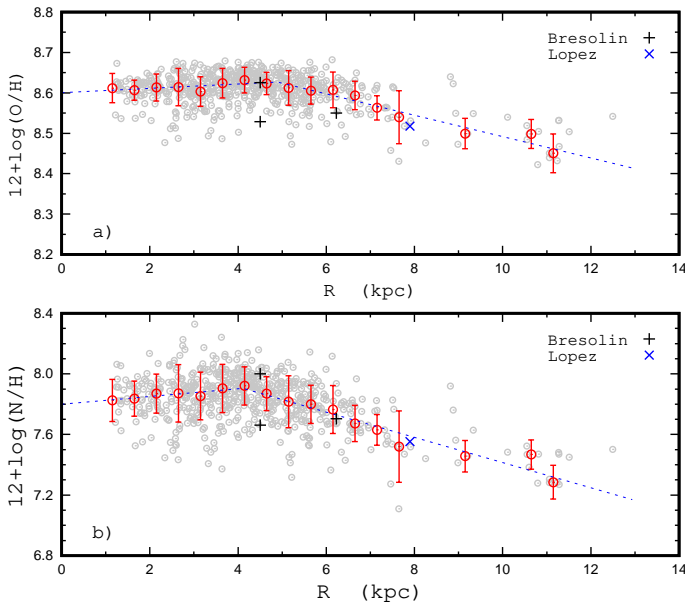


Fig. 7. Comparison between abundances in NGC 3521 based on fibre measurements here and abundances based on H II regions from the literature. *Panel a:* Radial oxygen abundance distribution. The grey circles denote the R calibration-based abundances for the individual fibres. The red circles denote the median values of the oxygen abundances in bins of 0.5 kpc in radius, and the bars show the scatter in O/H around the median value of each bin. The line shows the O/H – R relation for those data. The plus signs denote the abundances in H II regions measured by Bresolin et al. (1999). The cross marks the abundance in H II region measured by López et al. (2019). *Panel b:* Same as panel (a), but for the nitrogen abundances.

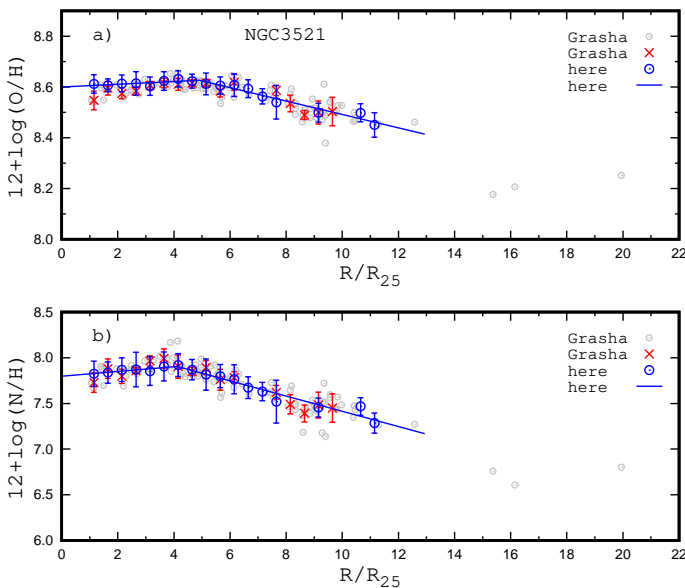


Fig. 8. Comparison between abundances in NGC 3521 based on fibre measurements here and abundances based on H II regions from Grasha et al. (2022). *Panel a:* Radial oxygen abundance distribution. The grey circles denote the R calibration-based abundances for the individual H II regions from Grasha et al. (2022), the red crosses denote the median values of the oxygen abundances in bins of 0.5 kpc in radius, and the bars show the scatter in O/H around the median value of each bin. The blue circles denote the median values of the oxygen abundances in bins for our fibre measurements, the line shows the O/H – R relation for those data (the same as in Fig. 4). *Panel b:* Same as panel (a), but for the nitrogen abundances.

be noted that only 5 out of the 578 fibres classified as H II region-like have $EW_{H\alpha} < 6 \text{ \AA}$.

We estimated the oxygen abundances in 573 fibres using the R calibration from Pilyugin & Grebel (2016). We also estimated the nitrogen-to-oxygen abundance ratios using the corresponding N/O calibration from Pilyugin & Grebel (2016) and then determined the nitrogen abundances using the relation $\log(N/H) = \log(O/H) + \log(N/O)$. The radial distributions of oxygen and nitrogen abundances for the individual spectra in the galaxy NGC 3521 are shown by grey points in panels (a) and (b), respectively, of Fig. 4. To minimise the effect of fibres with unreliable abundances in determining the radial abundance distribution, we used the median values of the abundances in bins of 0.5 kpc in radius (red circles in panels (a) and (b) of Fig. 4). Only bins with three or more points are considered. The binned O/H – R relation reveals a broken linear trend, described by the equations

$$\begin{aligned} 12 + \log(O/H) &= 8.600 + 0.0053 \times R, & R < 4.9 \\ &(\pm 0.007) &(\pm 0.0023), \\ &= 8.756 - 0.0264 \times R, & R > 4.9 \\ &(\pm 0.019) &(\pm 0.0024), \end{aligned} \quad (1)$$

shown by the line in panel (a) of Fig. 4. The broken linear N/H – R relation

$$\begin{aligned} 12 + \log(N/H) &= 7.799 + 0.0255 \times R, & R < 4.1 \\ &(\pm 0.020) &(\pm 0.0079), \\ &= 8.245 - 0.0831 \times R, & R > 4.1 \\ &(\pm 0.052) &(\pm 0.0070), \end{aligned} \quad (2)$$

is shown by the line in panel (b) of Fig. 4. It should be noted that the abundance measurements are not available at the very centre of NGC 3521 (within ~ 1 kpc) and near the optical radius (within ~ 1.5 kpc) (see Fig. 4). Then the central abundance and abundance at the optical radius are extrapolated values, determined using Eq. 1 and Eq. 2.

The coefficients in Eq. 1 (and Eq. 2) and the value of the break radius are derived using an iterative procedure. In the first step, the value of R_b is chosen by visual inspection of the radial abundance distribution, and the coefficients are determined by the best fit. Then a new value of the break radius is determined as the radius where the abundance estimated using the relation for the inner part is equal to the abundance obtained with the relation for the outer part, and the new coefficients are determined by the best fit. The iteration is stopped when the obtained values of R_b in successive steps agree within 0.01 kpc. The uncertainty of the break radius is estimated in the following way. A random noise ($\alpha \times$ uncertainty of coefficient) is added to each coefficient in Eq. 1 (and Eq. 2), where α is a random number from -1 to 1 . The value of the break radius is determined with the disturbed coefficients and its difference with the break radius for the undisturbed coefficients dR_b is obtained. The mean difference $\left(\frac{1}{n} \sum_{j=1}^n (dR_{b,j})^2\right)^{1/2}$ for 1000 simulations is considered as the uncertainty in the break radius. We found that the uncertainty in the break radius $R_{b,OH}$ in the O/H – R relation is 0.5 kpc and the uncertainty in the break radius $R_{b,NH}$ in the N/H – R relation is 0.4 kpc.

The validity of the shape of the oxygen abundance gradient in the galaxy can be verified by comparing it with the variation in the nitrogen emission line N_2 intensity across the disc of the galaxy (Pilyugin & Tautvaišienė 2024). The standard notation for nitrogen line intensities $N_2 = I_{[N II]\lambda 6548 + \lambda 6584} / I_{H\beta}$ is used. The intensity of the N_2 line correlates with the electron temperature in the nebula (e.g. Pilyugin & Grebel 2016) and, consequently, with oxygen abundance. In particular, it is

assumed within the framework of the N_2 calibration that the oxygen abundance is a function solely of the intensity of the N_2 line (Pettini & Pagel 2004; Marino et al. 2013). It should be emphasised that the value of N_2 alone does not provide an accurate abundance determination of H II regions, and the N/O ratio and the excitation parameter must also be considered (Pilyugin & Grebel 2016; Schaefer et al. 2020). Panel (c) in Fig. 4 shows the variation in N_2 intensity across the disc of NGC 3521. The similarity between the radial oxygen abundance distribution (panel (a) in Fig. 4) and the radial variation in N_2 intensity (panel (c) in Fig. 4) confirms the validity of the shape of the oxygen abundance gradient in NGC 3521.

To examine the influence of the chosen positions of the centres of the bins on the derived parameters of the oxygen and nitrogen abundance distributions, we considered these gradients for ten positions of the centres of the bins. The position of the centre of j -th bin, $R_{cb,j}$, is $R_{cb,j} = R_{cb,1} + (j - 1) \times (\text{bin size})$, where the bin size is equal to 0.5 kpc. We considered ten variants of the position of the first bin centre from $R_{cb,1} = 0$ to $R_{cb,1} = 0.45$ kpc with the step of 0.05 kpc. Figure 5 shows the derived parameters of the abundances distributions as a function of the position of the first bin centre: the mean value of the deviations of the binned oxygen abundances around the obtained broken O/H – R relation (panel (a)), the derived values of the central oxygen abundance (panel (b)), the oxygen abundance at the optical radius (panel (c)), and the values of the break radii in the O/H – R distributions (circles) and in the N/H – R distributions (crosses) (panel (d)). Panel (b) in Fig. 5 shows that the derived value of the central oxygen abundance depends weakly on the adopted positions of the centres of the bins; the difference between the values of $(\text{O}/\text{H})_0$ for any two values of the $R_{cb,1}$ is within 0.025 dex. Similarly, panel (c) shows that the derived value of the oxygen abundance at the optical radius also depends weakly on the adopted positions of the centres of the bins; again, the difference between the values of $(\text{O}/\text{H})_{R_{25}}$ for any two values of $R_{cb,1}$ is within 0.025 dex. Panel (d) of Fig. 5 shows that the values of the break radius in the O/H – R distributions estimated for different $R_{cb,1}$ can differ by more than 1 kpc, from $R_{b,OH} = 4.56$ kpc for $R_{cb,1} = 0.35$ kpc to $R_{b,OH} = 5.77$ kpc for $R_{cb,1} = 0.05$ kpc. The values of the break radius in the N/H – R distributions estimated for different $R_{cb,1}$ can change within 0.5 kpc, from $R_{b,NH} = 4.05$ kpc for $R_{cb,1} = 0.25$ kpc to $R_{b,NH} = 4.46$ kpc for $R_{cb,1} = 0.05$ kpc. It should be noted that the $R_{b,NH}$ is smaller than the $R_{b,OH}$ for each value of the $R_{cb,1}$, but the difference is less than the uncertainties of these values. Panel (a) in Fig. 5 shows that the mean value of the deviations of the binned oxygen abundances around the obtained broken O/H – R relation is between $\sigma_{OH} = 0.010$ and $\sigma_{OH} = 0.018$ dex, with one exception for the case of $R_{cb,1} = 0.20$ kpc. Thus, the abundances at the centre and optical radius depend weakly on the bin position, while the breaking radii and their uncertainties can exhibit greater variability. Notably, $R_{b,OH} > R_{b,NH}$ for any tested bin position, although the differences are comparable to the uncertainties. We use the distribution with minimum value of the σ_{OH} (the case of $R_{cb,1} = 0.15$ kpc, $\sigma_{OH} = 0.0105$ dex) in our discussion of the abundances distribution in the NGC 3521. These distributions are shown in Fig. 4 and are approximated by Eq. 1 and Eq. 2.

To assess the effect of the chosen ε limit on the derived oxygen and nitrogen abundance distributions, we computed these gradients using a stricter limit of $\varepsilon = 0.15$. The necessary emission lines in 202 H II region-like spectra satisfy the condition $\varepsilon \lesssim 0.15$. The grey points in panel (a) of Fig. 6 denote the oxygen abundances in individual fibres, and the red circles indicate the

binned values of the abundances for fibres selected using $\varepsilon \lesssim 0.15$. The line in panel (a) of Fig. 6 shows the O/H – R relation for $\varepsilon < 0.30$ (from panel (a) of Fig. 4, Eq. 1). Panel (b) of Fig. 6 shows a similar diagram for the nitrogen abundances. Both panels show that binned values for $\varepsilon \lesssim 0.15$ closely follow the O/H – R and N/H – R relations derived with $\varepsilon \lesssim 0.30$. This consistency suggests that measurement errors in the fibre spectra are random. Thus, a sample of fibres selected with $\varepsilon \lesssim 0.3$ provides a reliable estimate of the radial oxygen and nitrogen abundance distributions in the disc of NGC 3521.

The spectra of the H II regions in NGC 3521 were measured by Zaritsky et al. (1994), Bresolin et al. (1999), and López et al. (2019). Unfortunately, Zaritsky et al. (1994) did not measure the fluxes of the nitrogen emission line $[\text{N II}]\lambda 6584$ required for the abundance determination through the R calibration. We estimated the oxygen and nitrogen abundances for three H II regions using the line measurements from Bresolin et al. (1999). The galactocentric distances of those H II regions were determined using the R/R_{25} values reported in Zaritsky et al. (1994). These H II regions are overlaid as plus signs on the O/H – R (panel (a) of Fig. 7) and on the N/H – R (panel (b) of Fig. 7) diagrams. López et al. (2019) investigated an H II region near an ultraluminous X-ray source (ULX) in NGC 3521, located ~ 105 pc to the NE; this distance was rescaled adopting the distance to NGC 3521 used here, $d = 10.7$ Mpc, from the $d = 14.29$ Mpc used by López et al. (2019). We estimated the oxygen and nitrogen abundance in this H II region through the R calibration using their line measurements. The galactocentric distance of the H II region is determined using the ULX source coordinates reported by López et al. (2017). This H II region is overlaid as a cross on the O/H – R (panel (a) of Fig. 7) and on the N/H – R (panel (b) of Fig. 7) diagrams. Figure 7 shows that the abundance in H II regions measured by Bresolin et al. (1999) and by López et al. (2019) align with the distribution of abundances derived from the fibre spectra in this study.

It was noted above that the spectra of 92 H II regions in NGC 3521 were measured by Grasha et al. (2022). So the fluxes of the emission lines required for the abundance determination through the R calibration are available. We estimated the oxygen and nitrogen abundances for those H II regions using the line measurements from Grasha et al. (2022). The galactocentric distances of those H II regions were determined using the position angle of the major axis and the inclination angle obtained here. The R calibration-based oxygen abundance as a function of the radius for individual H II regions is shown by the grey circles in panel (a) of Fig. 8. The red crosses denote the median values of the oxygen abundances in bins of 0.5 kpc in radius, and the bars show the scatter in O/H around the median value of each bin. The blue circles denote the median values of the oxygen abundances in bins for our fibre measurements; the line shows the O/H – R relation for those data (from Fig. 4). A close inspection of panel (a) of Fig. 8 shows that the binned oxygen abundances for the H II regions measured by Grasha et al. (2022) and the binned oxygen abundances for the fibres measured here agree within the uncertainties. Panel (b) of Fig. 8 shows a similar comparison for nitrogen abundances. A close examination of panel (b) of Fig. 8 shows again that the binned nitrogen abundances for the H II regions measured by Grasha et al. (2022) and the binned nitrogen abundances for the fibres measured here agree within the uncertainties.

Thus, the oxygen abundance in the inner region of the disc of NGC 3521 (within $R_{b,OH}$) remains nearly constant, while the oxygen abundance gradient is negative at larger radii (panel (a) of Fig. 4 and Eq. 1). The nitrogen abundance shows a similar

pattern. The break in the O/H distribution occurs at a smaller radius than the O/H distribution break (panel (b) of Fig. 4 and Eq. 2), but the difference between $R_{b,OH}$ and $R_{b,NH}$ is within the uncertainties of these values. Some spiral galaxies show a similar behaviour of the oxygen and nitrogen abundances with radius (e.g. Kreckel et al. 2019; Pilyugin & Tautvaišienė 2024). Kreckel et al. (2019) have determined the gas phase oxygen abundances for H II regions across the discs of eight nearby galaxies using Very Large Telescope/Multi Unit Spectroscopic Explorer (MUSE) optical integral field spectroscopy as part of the PHANGS-MUSE survey. One of these galaxies (NGC 4254) shows a flattening in the oxygen abundance distribution in the inner part of the disc with the break radius of $R_{b,OH} \sim 0.2R_{25}$. A sample of 60 well-measured spiral galaxies from the MaNGA survey with different shapes of radial oxygen abundance distributions was examined in Pilyugin & Tautvaišienė (2024). It was found that 23 of the 60 galaxies belong to the sequence of galaxies with level-slope (LS) gradients, where the oxygen abundance in the inner region of the disc is nearly constant (the gradient is flatter than $-0.05 \text{ dex}/R_{25}$) and decreases at larger radii. The scatter of the binned oxygen abundances around the broken O/H– R relation is smaller than $\sim 0.01 \text{ dex}$. The radial nitrogen abundance distributions in the majority of galaxies with LS-type distributions show breaks at smaller radii than the O/H distribution breaks.

It was shown in Pilyugin & Tautvaišienė (2024) that such observed behaviour of oxygen and nitrogen abundances, constant levels in the inner disc and negative gradients at larger radii, with nitrogen breaks occurring at smaller radii than oxygen, can be naturally explained by accounting for the time delay between nitrogen and oxygen enrichment (see e.g. Fig. 1 in Maiolino & Mannucci 2019), and the variation in the star formation history along the radius predicted by the inside-out disc evolution model (e.g. Matteucci & Francois 1989). The nearly constant oxygen abundance in the inner region $R < R_{b,OH}$, panel (a) in Fig. 4, suggests that after the region has reached a high astration level some time ago $\tau(R)$, the star formation rate in the region decreases. The short-living massive stars in this region will produce relatively small amounts of oxygen. At the same time the production of nitrogen by long-living low-mass stars from the previous generations of stars continues. The increase in the nitrogen abundance as the radius decreases in the zone of constant oxygen abundance (within $R_{b,OH} \gtrsim R \gtrsim R_{b,NH}$) suggests that the number of nitrogen-producing stars from previous generations, which have enough time to complete their evolution and eject their nitrogen into the interstellar medium, increases as the radius decreases; that is, the value of $\tau(R)$ increases as the radius decreases. The value of $\tau(R)$ becomes high enough at radius $R_{b,NH}$ that a bulk of nitrogen-producing stars from previous generations complete their evolution; the nitrogen abundance then reaches a high level at $R_{b,NH}$ and remains nearly constant at $R < R_{b,NH}$. Thus, the observed behaviour of oxygen and nitrogen abundances with radius in NGC 3521 clearly supports the inside-out disc evolution model, where the galactic centre of the galaxy evolves more rapidly than the outer regions (Matteucci & Francois 1989). The radial distributions of oxygen and nitrogen abundances obtained here provide evidence that NGC 3521 is a typical LS-gradient galaxy.

4. Comparison between NGC 3521 and the Milky Way

A comparison between the global structural characteristics of NGC 3521 and the Milky Way is given in McGaugh (2016) and

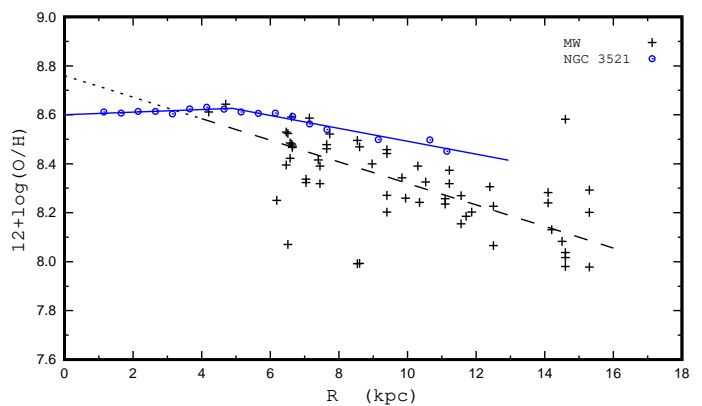


Fig. 9. Comparison between radial oxygen abundance distributions in NGC 3521 and the Milky Way. The plus signs denote the abundances in the H II regions of the Milky Way, and the dashed line is the O/H– R relation adopted for the Milky Way. The circles mark the binned abundances in NGC 3521 (from panel (a) of Fig. 4). The solid line shows the O/H– R relation adopted for NGC 3521, Eq. 1.

Pilyugin et al. (2023). These studies reveal a remarkable agreement between the key parameters in the two galaxies: the optical radius of the MW is $R_{25} = 12 \text{ kpc}$ versus $R_{25} = 12.94 \text{ kpc}$ for NGC 3521; the stellar mass of the MW is $\log(M_*/M_\odot) = 10.716$ versus $\log(M_*/M_\odot) = 10.70$ for NGC 3521; the rotation velocity of the MW is $V_{rot} = 235 \text{ km s}^{-1}$ versus $V_{rot} = 227 \text{ km s}^{-1}$ for NGC 3521; the mass of the central supermassive black hole in the MW is $\log(M_{BH}/M_\odot) = 6.618$ versus $\log(M_{BH}/M_\odot) = 6.85 \pm 0.58$ in NGC 3521. This illustrates that the galaxy NGC 3521 has structural parameters that are very similar to those of the MW, which means that NGC 3521 is a nearly structural analogue of the Milky Way. Here we compare the radial distributions of the oxygen abundances, the gas mass fractions, and the effective oxygen yields (indicators of the evolutionary stage) of NGC 3521 and the Milky Way.

4.1. Oxygen abundance

The radial distribution of the gas-phase oxygen abundances in the Milky Way was determined in a number of investigations (e.g. Shaver et al. 1983; Deharveng et al. 2000; Rudolph et al. 2006; Fernández-Martín et al. 2017; Arellano-Córdova et al. 2020, 2021). The electron temperatures and ionic abundances in the MW H II regions are usually determined using the measurements of the optical emission lines. However, the observations of the radio recombination lines were used in the determination of the electron temperatures in the H II regions by Shaver et al. (1983) and Deharveng et al. (2000), and the measurements of the far-IR emission lines were used in the ionic abundances determinations by Rudolph et al. (2006). A mandatory condition of the current study is that the abundances in the MW and in NGC 3521 are determined using the same metallicity scale. We considered a sample of 41 H II regions of the MW from Arellano-Córdova et al. (2020) and Arellano-Córdova et al. (2021). The electron temperatures and ionic abundances in these H II regions were determined using the measurements of the optical emission lines. However, the original T_e -based oxygen abundances of the H II regions were not used in this study; instead, they were re-estimated for the following reason: the oxygen abundances in the H II regions of the MW are being compared to those of NGC 3521 determined through the R calibration from Pilyugin & Grebel (2016). The

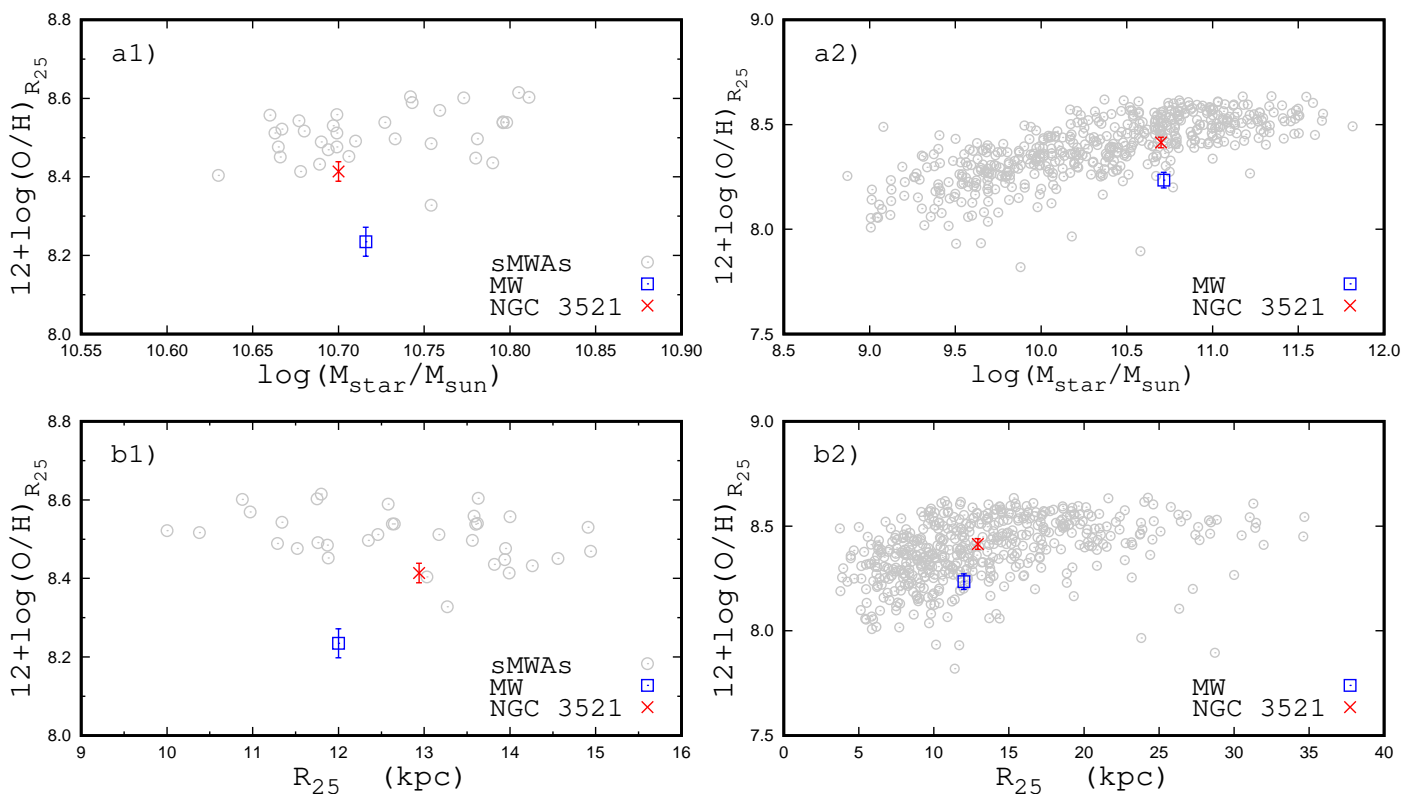


Fig. 10. Comparison of the oxygen abundance at the optical radius in the Milky Way and in the structural Milky Way analogues. *Panel a1:* Oxygen abundance at the optical radius of the galaxy as a function of its stellar mass. The grey circles designate the structural Milky Way analogues, the square marks the Milky Way, and the cross is the NGC 3521. *Panel a2:* Same as panel (a1), but the grey circles show a total sample of galaxies from Pilyugin et al. (2023) (not only the structural Milky Way analogues). *Panel b1:* Oxygen abundance at the optical radius of the galaxy as a function of the optical radius. The designations are the same as in panel (a1). *Panel b2:* Same as panel (b1), but the grey circles show a total sample of galaxies.

T_e -based oxygen abundances of the H II regions, used as calibrating data points in the construction of the R calibration, were derived using the T_e -method equations reported in Pilyugin et al. (2012). To ensure that the Milky Way oxygen abundances correspond to the same metallicity scale as the R calibration-based abundances in NGC 3521, the oxygen abundances in the Milky Way H II regions were re-calculated using the same T_e -method equations from Pilyugin et al. (2012).

The line intensity measurements in the spectra of H II regions are from the same sources as those in Arellano-Córdova et al. (2020) and Arellano-Córdova et al. (2021). If the measurements of two auroral lines ($[\text{O III}]\lambda 4363$ and $[\text{N II}]\lambda 5755$) are available for the H II region, then two values of the oxygen abundance are determined. The first value of the abundance is based on the electron temperature in the high-ionisation part of the nebula t_3 estimated using the auroral line $[\text{O III}]\lambda 4363$, while the electron temperature in the low-ionisation zone (t_2) is obtained through the canonical relationship between t_2 and t_3 : $t_2 = 0.7t_3 + 0.3$ (Campbell et al. 1986; Garnett 1992). The second value of the abundance is based on the electron temperature in low-ionisation zone estimated from the measured auroral line $[\text{N II}]\lambda 5755$, and the electron temperature in high-ionisation zone is determined from the relationship between electron temperatures.

The oxygen abundances of individual H II regions in the Milky Way are shown by the plus signs in Fig. 9. The adopted $\text{O}/\text{H} - R$ relation in the Milky Way is given by

$$12 + \log(\text{O}/\text{H}) = 8.762(\pm 0.043) - 0.0439(\pm 0.0042) \times R \quad (3)$$

where R is the radius in kiloparsecs. This relation is shown by the dashed line in Fig. 9 in the radius range from 4 kpc to 16

kpc (where the measurements of the spectra of H II regions are available), an extrapolation of this relation to the centre of the Milky Way is shown by the dotted line. This $\text{O}/\text{H} - R$ relation gives an oxygen abundance at the optical radius ($R_{25} = 12$ kpc) of $12 + \log(\text{O}/\text{H})_{R_{25}} = 8.235$. The binned oxygen abundances in the disc of NGC 3521 (from panel (a) of Fig. 4) are shown by circles in Fig. 9. The $\text{O}/\text{H} - R$ relation in NGC 3521 (Eq. 1) is shown by the solid line in Fig. 9, yielding an oxygen abundance of $12 + \log(\text{O}/\text{H})_{R_{25}} = 8.414$ at the optical radius ($R_{25} = 12.94$ kpc) of NGC 3521.

Figure 9 shows that the oxygen abundances of the two H II regions nearest to the centre of the Milky Way (at galactocentric distances of 4-5 kpc) are close to the binned oxygen abundances in NGC 3521 at the same galactocentric distances. The lack of abundance measurements in the central region of the Milky Way prevents an accurate determination of the oxygen abundance at the centre. An extrapolation of the linear $\text{O}/\text{H} - R$ relation to the very centre of the Milky Way may be unjustified since the radial oxygen abundance distribution in the Milky Way can show a flattening in the central part (e.g. Arellano-Córdova et al. 2020). However, a definitive conclusion on the flattening of the oxygen abundance gradient in the central part of the Milky Way can only be made based on the abundance determinations of H II regions close to the centre. Thus, the oxygen abundance in NGC 3521 is close to that of the Milky Way at the radii of 4-5 kpc (near the radius break in the $\text{O}/\text{H} - R$ relation for NGC 3521) and the oxygen abundance in NGC 3521 is higher than in the Milky Way at larger radii.

Table 1. Parameters of the radial distributions of the surface mass density of atomic H I and molecular H₂ hydrogen in the Milky Way (the coefficients in Eq. 4).

	R_d (kpc)	R_m (kpc)	Σ_0 (M_\odot/pc^2)
H I+He	7	4	53.1
H ₂ +He	1.5	12	2180

Panels (a1) and (b1) in Fig. 10 show the comparison between the oxygen abundance at the optical radius in the Milky Way and the structural Milky Way analogues from Pilyugin et al. (2023). Panels (a1) and (b1) in Fig. 10 show that the oxygen abundances at the optical radius of the Milky Way are lower than those in NGC 3521 and any other structural Milky Way analogues. It should be noted that the oxygen abundances at the optical radii of some spiral galaxies (which are not sMWAs) are lower than in the Milky Way (panels (a2) and (b2) in Fig. 10). For example, the R calibration-based oxygen abundance at the optical radius in the well-studied giant spiral galaxy M 101 (e.g. Kennicutt & Garnett 1996; Pilyugin 2001; Kennicutt et al. 2003; Croxall et al. 2016) is $12 + \log(\text{O}/\text{H}) \sim 7.9$, which is lower by a factor of around two than in the Milky Way. The oxygen abundance at the optical radius of NGC 3521 is lower than that of most sMWAs (panels (a1) and (b1) in Fig. 10). The difference between the abundances at the optical radius between NGC 3521 and the Milky Way is smaller than that of most sMWAs. NGC 3521, being the nearest structural analogue of the Milky Way, is also among the galaxies that show the smaller differences to the Milky Way in the oxygen abundances at the optical radius, although the difference is as large as 0.17 dex.

Thus, to make a solid conclusion on the discrepancy (or similarity) between the central oxygen abundances in NGC 3521 and the Milky Way, the abundance determinations of H II regions near the centre of the Milky Way should be performed. The oxygen abundance in the Milky Way is closer to that of NGC 3521 at the radii of 4-5 kpc (near the radius break in the O/H – R relation for NGC 3521). The oxygen abundances in the outer part of the Milky Way are lower than those in the outer part of NGC 3521; the difference in the oxygen abundances at the optical radius is as large as ~ 0.17 dex. The lower oxygen abundances in the outer part of the Milky Way in comparison to NGC 3521 can be caused by the following: a higher gas mass fraction in the outer part of the Milky Way, an inflow of a larger amount of low-metallicity gas, and a higher efficiency of the heavy element loss through Galactic winds in the outer part of the Milky Way compared to the outer part of NGC 3521. We compare the radial distributions of the gas mass fraction in the Milky Way and in NGC 3521 in the following section.

4.2. Gas mass fraction

Here we compare the radial distributions of the gas mass fraction μ or the astration level s across the Milky Way and NGC 3521. The value of the astration level s indicates the fraction of the gas converted into stars, $s = M_\star / (M_\star + M_{\text{gas}})$, that is $s = 1 - \mu$. The mass surface densities of the atomic gas, molecular gas, and stars as a function of the radius in NGC 3521 were taken from Leroy et al. (2008), where the surface densities are corrected for inclination and a factor of 1.36 is used in the determination of atomic and molecular gas densities to account for helium. The gas mass surface density as a function of radius in NGC 3521

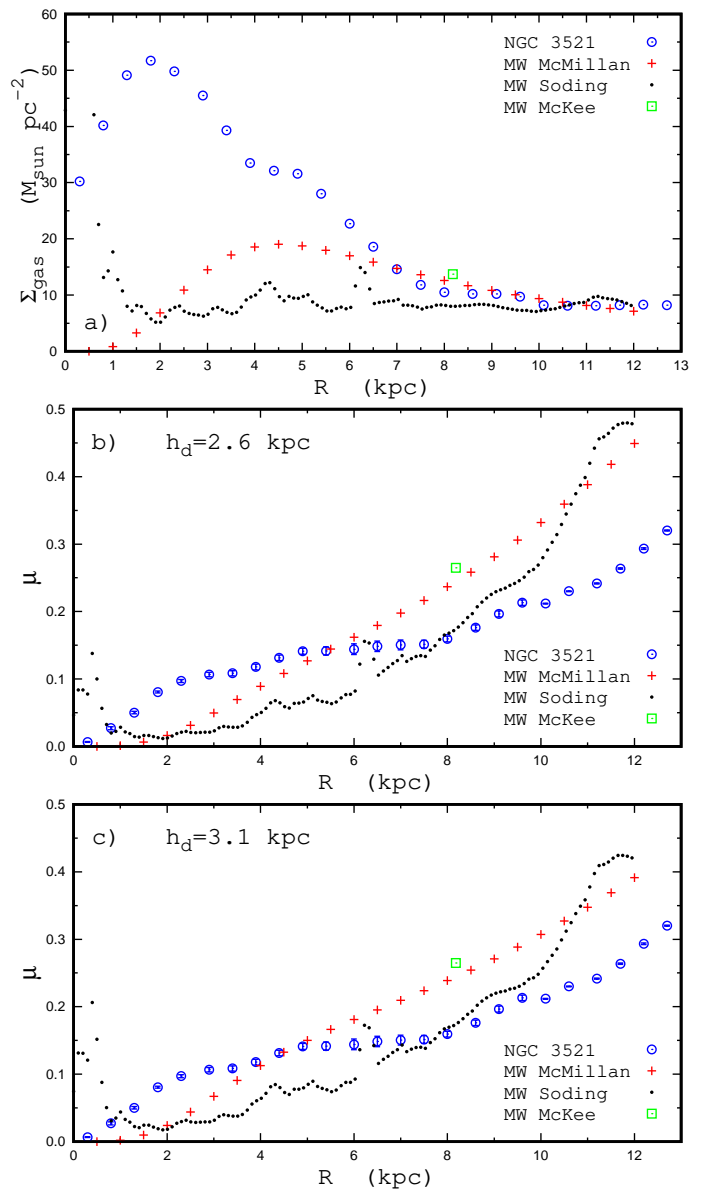


Fig. 11. Comparison between the radial distributions of the gas mass surface density and the gas mass fraction in NGC 3521 and the Milky Way. *Panel a:* Radial distributions of the gas mass surface density in NGC 3521 and the Milky Way. The circles designate the gas mass surface densities in NGC 3521. The plus signs show the gas mass surface densities in the Milky Way from McMillan (2017). The points are the gas mass surface densities in the Milky Way from Soding et al. (2024). The square marks the gas mass surface density in the solar vicinity from McKee et al. (2015). *Panel b:* Radial distributions of the gas mass fraction in NGC 3521 and the Milky Way. The gas mass fractions in NGC 3521 are shown by the circles; the bars display the uncertainties (the bars are usually smaller than the symbol size). The gas mass fractions in the Milky Way were estimated with the stellar disc scale length of $h_d = 2.6$ kpc and the gas mass surface densities shown in panel (a). The notations are the same as in panel (a). *Panel c:* Same as panel (b), but for the stellar disc scale length of $h_d = 3.1$ kpc.

is shown by the circles in panel (a) of Fig. 11, and the gas mass fraction as a function of radius is shown by the circles in panels (b) and (c) of Fig. 11. The uncertainty of the obtained values of the gas mass fraction at a given radius is estimated in the following way. A random noise ($\alpha \times$ uncertainty) is added to the mass surface densities of the atomic gas, molecular gas, and stars (whose values and their uncertainties are from Leroy et al.

2008), where α is a random number from -1 to 1 . The value of μ is estimated from the disturbed surface densities, and its difference with the gas mass fraction for the undisturbed surface densities is determined. The mean difference for 1000 simulations is considered as the uncertainty of the value of the gas mass fraction. The obtained uncertainties of the values of the gas mass fraction in NGC 3521 are shown by bars in panels (b) and (c) of Fig. 11.

The radial distributions of the surface mass density of atomic H I and molecular H₂ hydrogen in the Milky Way are discussed in many investigations (e.g. Dame 1993; Kalberla & Dedes 2008; Nakanishi & Sofue 2016; Marasco et al. 2017; McMillan 2017; Bacchini et al. 2019; Mertsch & Phan 2023; Söding et al. 2024). We considered two of the most different distributions for the surface gas mass density in the Milky Way. The widely used radial distribution of the surface gas mass density from McMillan (2017) is based on the investigations of Dame (1993) and Kalberla & Dedes (2008), the distributions of the surface mass density of atomic H I and molecular H₂ hydrogen (including helium) are approximated by the expression

$$\Sigma_{H+He} = \Sigma_0 \exp\left(-\frac{R_m}{R} - \frac{R}{R_d}\right). \quad (4)$$

The coefficients Σ_0 , R_m , and R_d for atomic H I and molecular H₂ hydrogen are given in Table 1. The radial distribution of the gas mass surface density in the Milky Way from McMillan (2017) is shown by the plus signs in panel (a) of Fig. 11. We also considered the radial distribution of the hydrogen surface mass density from Söding et al. (2024). We added the helium contribution (a factor of 1.36) to the original surface hydrogen mass density. The radial distribution of the gas mass surface density in the Milky Way from Söding et al. (2024) is shown by the dark points in panel (a) of Fig. 11. The gas mass surface density in the solar vicinity ($13.7 \pm 1.6 M_\odot \text{ pc}^{-2}$) from McKee et al. (2015) is shown by the square in panel (a) of Fig. 11. It should be noted that if the radial distribution obtained by McMillan (2017) is an adequate description of the gas mass surface density in the Milky Way, then the gas mass surface density in the solar vicinity is close to the azimuthally averaged surface mass density of the gas ($12.6 M_\odot \text{ pc}^{-2}$) at the solar galactocentric distance. If the radial distribution obtained by Söding et al. (2024) adequately describes the gas mass surface density in the Milky Way, then the gas mass surface density in the solar vicinity significantly exceeds the azimuthally averaged surface mass density of gas ($8.1 M_\odot \text{ pc}^{-2}$) at the solar galactocentric distance.

The radial distribution of the surface stellar mass density in the Milky Way disc is described by the expression

$$\Sigma_\star = \Sigma_{\star, R_0} \exp\left(-\frac{R - R_0}{h_d}\right), \quad (5)$$

where Σ_{\star, R_0} is the surface stellar mass density at the solar galactocentric distance ($R_0 = 8.178 \pm 0.013$ kpc, Gravity Collaboration 2019) and h_d is the disc scale length. Flynn et al. (2006) found a local stellar disc surface density of $35.5 M_\odot/\text{pc}^2$, while McKee et al. (2015) found the value of $33.4 M_\odot/\text{pc}^2$. The solar neighbourhood is located in the interarm region, and the ‘counted’ local stellar disc surface density should be corrected for the spiral arm enhancement in order to find the azimuthal average of the surface stellar mass density at the solar galactocentric distance, which means that a 10% enhancement should be added to the counted local stellar disc surface density (Flynn et al. 2006; Kubryk et al. 2015). This results in a stellar disc surface density at the

solar galactocentric distance of $39 M_\odot/\text{pc}^2$ (Flynn et al. 2006) and $37 M_\odot/\text{pc}^2$ (McKee et al. 2015). We adopted $\Sigma_{\star, R_0} = 38 M_\odot/\text{pc}^2$. Bland-Hawthorn & Gerhard (2016) analysed 130 papers on disc parameters, with scale lengths ranging from 1.8 to 6.0 kpc. Their analysis of the main papers (15 in all) on this topic led to $h_d = 2.6 \pm 0.5$ kpc.

The radial distribution of the gas mass fraction in the Milky Way obtained using the distribution of the surface stellar mass densities for the adopted disc scale length of 2.6 kpc and the radial distribution of the surface gas mass density from McMillan (2017), is shown by the plus signs in panel (b) of Fig. 11. The radial distribution of the gas mass fraction obtained using the radial distribution of the surface gas mass density from Söding et al. (2024) is shown by the points. The square in panel (b) of Fig. 11 marks the gas mass fraction in the solar vicinity estimated using the values of the gas mass surface density from McKee et al. (2015). To examine the influence of the disc scale length on the radial distribution of surface stellar mass densities and its effect on the radial distribution of gas mass fractions, we computed the radial distributions of gas mass fraction for a disc scale length of $h_d = 3.1$ (panel (c) of Fig. 11).

Figure 11 shows that the gas mass fraction in the Milky Way determined with the surface gas mass density from McMillan (2017) is lower than the gas mass fraction of NGC 3521 in the inner part (at radii $\lesssim 5$ kpc) and higher in the outer part (at radii $\gtrsim 5$ kpc). The gas mass fraction in the Milky Way determined with the surface gas mass density from Söding et al. (2024) is lower than the gas mass fraction of NGC 3521 within the galactocentric distances from ~ 1 kpc to ~ 8 kpc, and higher in the central part (at radii $\lesssim 1$ kpc) and in the outer part (at radii $\gtrsim 8$ kpc). In the next section we examine whether the discrepancy in oxygen abundances between the outer parts of the Milky Way and NGC 3521 can be attributed to a difference in the gas mass fraction only or if variations in the efficiency of gas exchange with the surroundings also contribute to the O/H discrepancy.

4.3. Effective oxygen yield

The simple model of chemical evolution of galaxies predicts that the oxygen abundance of the interstellar matter of a galaxy is related to the gas mass fraction μ and the oxygen yield Y_O by the formula

$$Z_O = Y_O \ln\left(\frac{1}{\mu}\right) \quad (6)$$

(Pagel 2009; Matteucci 2012, and references therein), where Z_O is the oxygen abundance expressed in units of oxygen mass fraction relative to mass of the interstellar matter. This simple model is based on the following assumptions: (i) an instantaneous recycling approximation, (ii) the element yield is constant (independent of metallicity), (iii) the system evolves as a closed box (no matter exchange between the system and its surroundings). Assumptions (i) and (ii) are well justified for the oxygen evolution since the oxygen is a primary element (the production of the oxygen is independent of the stellar metallicity) and the production and the ejection of newly synthesised oxygen by massive stars takes place in a short time compared to the timescale of galactic evolution. The gas exchange between the system and its surroundings (infall of low-metallicity gas and/or gas loss through the galactic winds) results in the decrease in the oxygen abundance for a given value of the gas mass fraction compared to the closed-box model; that is, it mimics the lowering of the oxygen yield (e.g. Edmunds 1990; Pilyugin 1994). Therefore, the deviation of the effective yield estimated using the measured oxygen

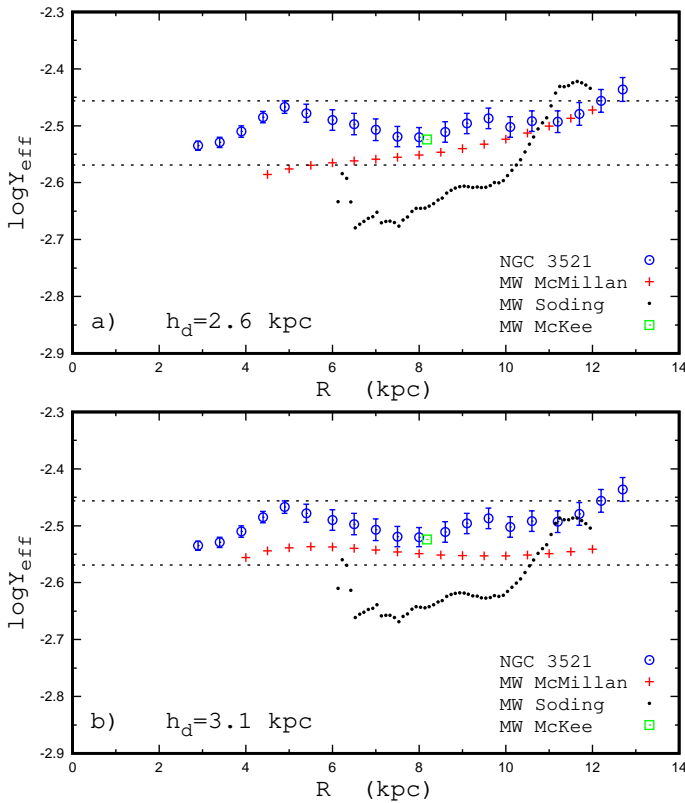


Fig. 12. Comparison between the effective oxygen yields in the NGC 3521 and the Milky Way for the radial oxygen abundance distributions shown in Fig. 9 and the gas mass fraction distributions displayed in Fig. 11. *Panel a*: The circles denote the effective oxygen yields in NGC 3521 as a function of radius and the bars show their uncertainties. The plus signs designate the radial distribution of the effective oxygen yields in the Milky Way based on the Σ_* with the stellar disc scale length of $h_d = 2.6$ kpc and on the Σ_{gas} from McMillan (2017); the points are the yields based on the Σ_{gas} from Söding et al. (2024). The square marks the effective oxygen yield in the solar vicinity based on the Σ_{gas} from McKee et al. (2015). The lines show the upper and lower values of the empirical estimations of the oxygen yield. *Panel b*: Same as panel (a), but for the stellar disc scale length of $h_d = 3.1$ kpc.

abundance Z_O and gas mass fraction μ

$$Y_{\text{eff}} = Z_O / \ln\left(\frac{1}{\mu}\right) \quad (7)$$

from the true oxygen yield Y_o can be used as an indicator of gas exchange between the system and its surroundings (e.g. Vílchez et al. 2019; Lara-López et al. 2019; Garduño et al. 2023). Empirical estimates of the oxygen yield Y_O for the metallicity scale defined by the H II regions with the T_e -based oxygen abundances (the abundances used in this study are compatible with this metallicity scale) result in $Y_O = 0.0027$ (Pilyugin et al. 2004), $Y_O = 0.0032$ (Bresolin et al. 2004), and between $Y_O = 0.0030$ and $Y_O = 0.0035$ depending on the amount of oxygen incorporated into the dust grains (Pilyugin et al. 2007).

Since the measured oxygen abundances are expressed in units of the number of oxygen atoms relative to hydrogen, while Z_O in Eq. (7) is in units of mass fraction, we adopt the following conversion equation for the oxygen (Garnett 2002):

$$Z_O = 12 \frac{O}{H}. \quad (8)$$

We note that the oxygen abundances determined using the emission line spectra are the gas-phase abundances.

Peimbert & Peimbert (2010) estimated the dust depletion of oxygen in Galactic and extragalactic H II regions and found that the fraction of oxygen atoms embedded in dust grains is a function of the oxygen abundance, which is about 0.12 dex for the metal-rich H II regions. This depletion has to be considered when the total (gas + dust) oxygen abundance is derived.

We estimate the values of the effective oxygen yields for different galactocentric distances within the optical radii in NGC 3521 and the Milky Way using the distributions of the gas mass fraction and the oxygen abundances described above. The simple model breaks down at low gas mass fractions because the term $\ln(1/\mu)$ blows up. Therefore, we do not estimate the effective oxygen yields for $\mu \lesssim 0.1$. Figure 12 shows the obtained values of the effective oxygen yield as a function of radius for NGC 3521 and the Milky Way. The lines mark the lower and upper values of the empirical estimations of the oxygen yield, $Y_O = 0.0027$ and $Y_O = 0.0035$. The uncertainty of the obtained value of the effective oxygen yield at a given radius is estimated in the following way. A random noise ($\alpha \times$ uncertainty) is added to each coefficient in the $O/H - R$ relation (Eq. 1) and to the mass surface densities of the atomic gas, molecular gas, and stars (these values and their uncertainties are from Leroy et al. 2008), where α is a random number from -1 to 1 . The value of the effective oxygen yield is estimated with the disturbed coefficients and its difference with the effective oxygen yield for undisturbed coefficients is determined. The mean difference for 1000 simulations is considered as the uncertainty of the value of the effective oxygen yield. The obtained uncertainties of the values of the effective oxygen yields in NGC 3521 are shown by the bars in Fig. 12.

Figure 12 shows that the obtained values of the effective oxygen yield in NGC 3521 are within the band outlined by the upper and lower values of the empirical estimations of the oxygen yield. The oxygen abundances in NGC 3521 are close to those predicted by the simple model for the chemical evolution of galaxies. This suggests that the mass exchange with the surroundings (the infall of low-metallicity gas and/or gas loss through the galactic winds) plays a small role, if any, in the current chemical evolution of NGC 3521.

The values of the Y_{eff} in the Milky Way obtained with the radial distribution of the gas mass surface density from McMillan (2017) are also between the upper and lower values of the empirical estimations of the oxygen yield. There is a systematic trend in Y_{eff} with radius in the Milky Way: the Y_{eff} slightly increases from the centre to the periphery in the case of the stellar disc scale length of $h_d = 2.6$ kpc (panel (a) in Fig. 12). The systematic trend in Y_{eff} with radius in the Milky Way disappears for the stellar disc scale length of $h_d = 3.1$ kpc, panel (b) in Fig. 12. The values of the Y_{eff} in the Milky Way obtained with the radial distribution of the gas mass surface density from Söding et al. (2024) are above the lower value of the empirical estimations of the oxygen yield near the optical radius, at radii larger than ~ 10.4 kpc (10.2 or 10.6 kpc depending on the adopted value of the stellar disc scale length). Moreover, the Y_{eff} values are above the upper value of the empirical estimations of the oxygen yield at radii larger than 11.1 kpc for the case of $h_d = 2.6$ kpc (panel (a) in Fig. 12). The Y_{eff} values are below the lower value of the empirical estimations of the oxygen yield at smaller radii. The effective yields are not estimated in the inner part of the Milky Way (at radii smaller than 6.1 kpc) because of the small value of gas mass fraction (the simple model breaks down at low gas mass fractions) or because of the oxygen abundances are not available.

It was noted above that the gas exchange between the system and the surroundings (infall of low-metallicity gas and/or gas loss through galactic winds) mimics the lowering of the oxygen yield. The values of the effective yields below the lower value of the empirical estimations of the oxygen yield obtained in the Milky Way at radii between ~ 6 and ~ 10.4 kpc for the radial distribution of the gas mass surface density from Söding et al. (2024) can be considered as evidence that mass exchange with the surroundings plays a significant role in the current evolution of this region in the Milky Way. It is important to note that the obtained value of the Y_{eff} in the solar vicinity (where the measurement of the gas mass fraction is the most accurate and, consequently, the estimation of the Y_{eff} is more reliable) is $Y_{eff} = 0.0030$; that is, the effective oxygen yield in the solar vicinity is in agreement with the empirical estimations of the oxygen yield.

Thus, the obtained values of the Y_{eff} in NGC 3521 are close to the Y_O ; that is, the oxygen abundances in NGC 3521 are close to those predicted by the simple model for the chemical evolution of galaxies. The values of the Y_{eff} in the outer part of the Milky Way obtained with the radial distribution of the gas mass surface density from McMillan (2017) are also close to the Y_O value; that is, the oxygen abundances in the Milky Way are close to those predicted by the simple model for the chemical evolution of galaxies. This is evidence that the mass exchange with the surroundings plays a small role, if any, in the current chemical evolution of the outer part of the Milky Way (similar to what is observed in NGC 3521).

The values of the Y_{eff} in the outer part of the Milky Way obtained with the radial distribution of the gas mass surface density from Söding et al. (2024) are more or less close to the empirical estimation of the oxygen yield near the optical radius, and are below the lower value of the empirical estimations of the oxygen yield at radii between ~ 6 and ~ 10.4 kpc. This can be considered as evidence that mass exchange with the surroundings can play a significant role in the chemical evolution of the outer part of the Milky Way, from ~ 6 to ~ 10.4 kpc. To make a solid conclusion of the role played by the mass exchange with the surroundings in the chemical evolution of the outer part of the Milky Way, it should be established which distribution of the surface gas mass density, McMillan (2017) or Söding et al. (2024), is a more adequate description of the gas distribution in the Milky Way. The obtained value of Y_{eff} in the solar vicinity (where the measurement of the gas mass fraction is the most accurate (McKee et al. 2015) and, consequently, the estimation of the effective oxygen yield is most reliable) is $Y_{eff} = 0.0030$, that is, the Y_{eff} in the solar vicinity is in agreement with the Y_O .

5. Conclusions

The IFU spectroscopy measurements of the galaxy NGC 3521 (structural Milky Way analogue) were carried out within the Metal-THINGS survey; the blue and red spectra were measured in the IFU fibres for three pointings. The radial distributions of the oxygen abundance, the gas mass fraction, and the effective oxygen yield in NGC 3521 were compared to that of the Milky Way, with the aim of examining the similarity (or disagreement) of their chemical evolutions.

We found that the oxygen abundance in the inner region of the disc of NGC 3521 is at a nearly constant level and the oxygen abundance gradient is negative at larger radii. The change in the nitrogen abundance with radius is similar to that for oxygen with the break in the N/H distribution at a smaller radius than the O/H distribution break, but the difference between the break radii is within the uncertainties of these values. The obtained radial dis-

tributions of the oxygen and nitrogen abundances in NGC 3521 are similar to those in other spiral galaxies with LS gradients (Pilyugin & Tautvaišienė 2024).

The oxygen abundances in the two H II regions nearest to the centre of the Milky Way (at galactocentric distances of 4-5 kpc) are close to the binned oxygen abundances in NGC 3521 at the same galactocentric distances. The central oxygen abundance in the Milky Way cannot be established due to the lack of relevant abundance measurements in H II regions near the centre. The oxygen abundances in the outer part of the Milky Way are lower than in the outer part of NGC 3521.

The oxygen abundance at the optical radius of NGC 3521 is lower than in the majority of other structural Milky Way analogues. The difference between the abundances at the optical radius of NGC 3521 and the Milky Way is smaller than in the majority of sMWAs, but the difference is as large as 0.17 dex.

The gas mass fraction in the outer part of NGC 3521 is lower than that in the Milky Way. The obtained values of the effective oxygen yield, Y_{eff} , in NGC 3521 are close to the empirical estimation of the oxygen yield, Y_O ; that is, the oxygen abundances in NGC 3521 are close to those predicted by the simple model for the chemical evolution of galaxies. This indicates that the mass exchange with its surroundings (the infall of low-metallicity gas and/or gas loss through galactic winds) plays a small role, if any, in the current chemical evolution of NGC 3521.

The values of the Y_{eff} in the MW obtained with the radial distribution of Σ_{gas} from McMillan (2017) are close to the value of Y_O . This indicates that the mass exchange with its surroundings also plays a small role in the chemical evolution of the MW, similarly to NGC 3521. The values of Y_{eff} in the MW obtained with Σ_{gas} from Söding et al. (2024) are more or less close to Y_O near the optical radius and are below Y_O at radii between ~ 6 and ~ 10.4 kpc. This suggests that the mass exchange with its surroundings plays a significant role in the chemical evolution of the outer part of the MW, in contrast to that in NGC 3521. To make a solid conclusion of the role of the mass exchange with the surroundings in the chemical evolution of the MW, it should be established which distribution of Σ_{gas} , from McMillan (2017) or from Söding et al. (2024), is a more adequate description of the gas distribution in the MW. The value of Σ_{gas} in the solar vicinity (McKee et al. 2015) is close to azimuthally averaged surface mass density of gas at the solar galactocentric distance in the distribution from McMillan (2017).

Acknowledgements. We are grateful to the referee for his/her constructive comments.

We thank Dr. K. Grasha for providing us with the measurements (emission line fluxes and coordinates) of their sample of H II regions in NGC 3521.

We thank L. Söding for providing us with the necessary numerical data on the radial distribution of the surface hydrogen density in the Milky Way.

LSP acknowledges support from the Research Council of Lithuania (LMTLT), grant no. P-LU-PAR-24-38.

MALL acknowledges support from the Spanish grant PID2021-123417OB-I00, and the Ramón y Cajal program funded by the Spanish Government (RYC2020-029354-I)

MEDR acknowledges support from PICT-2021-GRF-TI-00290 of Agencia I+D+i (Argentina).

We acknowledge the usage of the HyperLeda database (<http://leda.univ-lyon1.fr>).

References

Arellano-Córdova K.Z., Esteban C., García-Rojas J., Méndez-Delgado J.E., 2020, MNRAS, 496, 1051

- Arellano-Córdova K.Z., Esteban C., García-Rojas J., Méndez-Delgado J.E., 2021, *MNRAS*, 502, 225
- Asari, N. V., Cid Fernandes, R., Stasińska, G., et al. 2007, *MNRAS*, 381, 263
- Bacchini C., Fraternali F., Pezzulli G., et al., 2019, *A&A*, 632, A127
- Baldwin J.A., Phillips M.M., Terlevich R., 1981, *PASP*, 93, 5
- Begeman K.G., 1989, *A&A*, 223, 47
- Bland-Hawthorn J., Gerhard O., 2016, *ARA&A*, 54, 529
- Boardman N., Zasowski G., Seth A., et al., 2020a, *MNRAS*, 491, 3672
- Bresolin F., Kennicutt R.C., Garnett D.R., 1999, *ApJ*, 510, 104
- Bresolin F., Garnett D.R., Kennicutt R.C., 2004, *ApJ*, 615, 228
- Bruzual, G., & Charlot, S. 2003, *MNRAS*, 344, 1000
- Campbell A., Terlevich R., Melnick J., 1986, *MNRAS*, 223, 811
- Cardelli J.A., Clayton G.C., Mathis J.S., 1989, *ApJ*, 345, 245
- Cid Fernandes, R., Mateus, A., Sodre, L., Stasińska, G., & Gomes, J. M. 2005, *MNRAS*, 358, 363
- Cid Fernandes R., Stasińska G., Schlickmann M.S., et al., 2010, *MNRAS*, 403, 1036
- Cid Fernandes R., Stasińska G., Mateus A., Vale Asari N., 2011, *MNRAS*, 413, 1687
- Croxall K.V., Pogge R.W., Berg D.A., Skillman E.D., Moustakas J., 2016, *ApJ*, 830, 4
- D'Agostino J.J., Kewley L.J., Groves B.A., et al., 2019, *MNRAS*, 485, L38
- Daigle O., Carignan C., Amram P., et al., 2006, *MNRAS*, 367, 469
- Dame T.M., 1993, in Holt S.S., Verter F., eds, *American Institute of Physics Conference Series Vol. 278, Back to the Galaxy*. pp 267–278,
- Davis B.L., Berrier J.C., Johns L., et al., 2014, *ApJ*, 789, 124
- de Blok W.J.G., Walter F., Brinks E., et al., 2008, *AJ*, 136, 2648
- Deharveng L., Peña M., Caplan J., Costero R., 2000, *MNRAS*, 311, 329
- de Vaucouleurs G., Pence W.D., 1978, *AJ*, 83, 1163
- de Vaucouleurs G., de Vaucouleurs A., Corwin H.G., Buta R.J., Paturel J., Fouque P. 1991, *Third Reference Catalog of bright Galaxies*, New York: Springer Verlag (RC3)
- Edmunds M.G., 1990, *MNRAS*, 246, 678
- Fernández-Martín A., Pérez-Montero E., Vílchez J.M., Mampaso A., 2017, *A&A*, 597, A84
- Fielder C., Newman J.A., Andrews B.H., et al., 2021, *MNRAS*, 508, 4459
- Flynn C., Holmberg J., Portinari L., Fuchs B., Jahreiß H., 2006, *MNRAS*, 372, 1149
- Fraser-McKelvie A., Merrifield M., Aragón-Salamanca A., 2019, *MNRAS*, 489, 5030
- Garduño L.E., Zaragoza-Cardiel J., Lara-López M.A., et al., 2023, *MNRAS*, 526, 2479
- Garnett D.R., 1992, *AJ*, 103, 1330
- Garnett D.R., 2002, *ApJ*, 581, 1019
- Grasha K., Chen Q.H., Battisti A.J., et al., 2022, *ApJ*, 929, 118
- Gravity Collaboration, Abuter R., Amorim A., Bauböck M., et al., 2019, *A&A*, 625, 10
- Johnston V.D., Medling A.M., Groves B., et al., 2023, *ApJ*, 954, 77
- Hammer F., Puech M., Chemin L., Flores H., Lehnert M.D., 2007, *ApJ*, 662, 322
- Hill, G. J., MacQueen, P. J., Smith, M. P., et al. 2008, *Proc. SPIE*, 7014, 701470
- Kalberla P.M.W., Dedes L., 2008, *A&A*, 487, 951
- Kauffmann G., Heckman T.M., Tremonti C., et al. 2003, *MNRAS*, 346, 1055
- Kennicutt R.C., Garnett D.R., 1996, 456, 504
- Kennicutt R.C., Bresolin F., Garnett D.R., 2003, *ApJ*, 591, 801
- Kewley L.J., Dopita M.A., Sutherland R.S., Heisler C.A., Trevena J. 2001 *ApJ*, 556, 121
- Kewley L.J., Dopita M.A., 2002, *ApJS*, 142, 35
- Kreckel K., Ho I.-T., Blanc G.A., et al., 2019, *ApJ*, 887, 80
- Kubryk M., Prantzos N., Athanassoula E., 2015, *A&A*, 580, A126
- Lacerda E.A.D., Cid Fernandes R., Couto G.S., et al., 2018, *MNRAS*, 474, 3727
- Lang P., Meidt S.E., Rosolowsky E., et al., 2020, *ApJ*, 897, 122
- Lara-López M.A., De Rossi M.E., Pilyugin L.S., et al., 2019, *MNRAS*, 490, 868
- Lara-López M.A., Zinchenko I.A., Pilyugin L.S., et al. 2021, *ApJ*, 906, 42
- Lara-López M.A., Pilyugin L.S., Zaragoza-Cardiel J., et al., 2023, *A&A*, 669, A25
- Leroy A.K., Walter F., Brinks E., et al., 2008, *AJ*, 136, 2782
- Leroy A.K., Schinnerer E., Hughes A., et al., 2020, *ApJS*, 257, 43
- Licquia T.C., Newman J.A., Brinchmann J., 2015, *ApJ*, 809, 96
- Licquia T.C., Newman J.A., Bershady M.A., 2016, *ApJ*, 833, 220
- López K.M., Heida M., Jonker P.G., et al., 2017, *MNRAS*, 469, 671
- López K.M., Jonker P.G., Heida M., et al., 2019, *MNRAS*, 489, 1249
- Maiolino R., Mannucci F., 2019, *A&A Rev.*, 27, 3
- Makarov D., Prugniel P., Terekhova N., Courtois H., Vauglin I. 2014, *A&A*, 570, A13
- Marasco A., Fraternali F., van der Hulst J.-M., Oosterloo T., 2017, *A&A*, 607, 106
- Marino R.A., Rosales-Ortega F.F., Sánchez S.F., et al., 2013, *A&A*, 559, A114
- Matteucci F., 2012, *Chemical Evolution of Galaxies*. *Astronomy and Astrophysics Library*, Springer-Verlag Berlin Heidelberg, Germany 0
- Matteucci F., Francois P., 1989, *MNRAS*, 239, 885
- McGaugh S.S., 2016, *ApJ*, 816, 42
- McKee C.F., Parravano A., Hollenbach D.J., 2015, *ApJ*, 814, 13
- McMillan P.J., 2017, *MNRAS*, 465, 76
- Mertsch P., Phan V.H.M., 2023, *A&A*, 671, A54
- Mutch S.J., Croton D.J., Poole G.B., 2011, *ApJ*, 736, 84
- Nakanishi H., Sofue Y., 2016, *PASJ*, 68, 5
- Oh S.-H., Staveley-Smith L., Spekkens K., Kamphuis P., Koribalski B.S., 2018, *MNRAS*, 473, 3256
- Osterbrock D.E., Ferland G.J., 2006, *Astrophysics of Gaseous Nebulae and Active Galactic Nuclei*. University Sciences- Books, Mill Valley, CA
- Pagel B.E.J., 2009, *Nucleosynthesis and Chemical Evolution of Galaxies*. Cambridge University Press, Cambridge, UK.
- Peimbert A., Peimbert M., 2010, *ApJ*, 724, 791
- Pettini M., Pagel B.E.J., 2014, *MNRAS*, 348, L59
- Pilyugin L.S., 1994, *A&A*, 287, 387
- Pilyugin L.S., 2001, *A&A*, 373, 56
- Pilyugin L.S., Vílchez J.M., Contini T., 2004, *A&A*, 425, 849
- Pilyugin L.S., Thuan T.X., Vílchez J.M., 2007, *MNRAS*, 376, 353
- Pilyugin L.S., Grebel E.K., Mattsson L., 2012, *MNRAS*, 424, 2316
- Pilyugin L.S., Grebel E.K., 2016, *MNRAS*, 457, 3678
- Pilyugin L.S., Grebel E.K., Zinchenko I.A., Nefedyev Y.A., Vílchez J.M., 2019, *A&A*, 623, A122
- Pilyugin L.S., Grebel E.K., Zinchenko I.A., et al., 2020, *A&A*, 639, A96
- Pilyugin L.S., Cedrés B., Zinchenko I.A., et al., 2021, *A&A*, 653, A11
- Pilyugin L.S., Lara-López M.A., Vílchez J.M., et al., 2022, *A&A*, 668, A5
- Pilyugin L.S., Tautvaišienė G., Lara-López M.A., 2023, *A&A*, 676, A57
- Pilyugin L.S., Tautvaišienė G., 2024, *A&A*, 682, A41
- Rudolph A.L., Fich M., Bell G.R., et al., 2006, *ApJS*, 162, 346
- Sánchez S.F., Rosales-Ortega F.F., Iglesias-Páramo J., et al., 2014, *A&A*, 563, A49
- Sánchez S.F., Walcher C.J., Lopez-Cobá C., et al., 2021, *Rev. Mex. Astron. Astrofis.*, 57, 3
- Sánchez S.F., Lugo-Aranda A.Z., Sánchez Almeida J., et al., 2024, *A&A*, 682, A71
- Schaefer A.L., Tremonti C., Belfiore F., et al., 2020, *ApJL*, 890, L3
- Shaver P.A., McGee R.X., Newton L.M., Danks A.C., Pottasch S.R., 1983, *MNRAS*, 204, 53
- Skrutskie M.F., Cutri R.M., Stiening R., et al., 2006, *AJ*, 131, 1163
- Söding L., Edenhofer G., Enßlin T.A. et al., 2024, *astro-ph:2407.02859*
- Storey P.J., Zeppen C.J. 2000, *MNRAS*, 312, 813
- Vílchez J.M., Relaño M., Kennicutt R., et al., 2019, *MNRAS*, 483, 4968
- Walter F., Brinks E., de Blok W.J.G., et al., 2008, *AJ*, 136, 2563
- Warner P.J., Wright M.C.H., Baldwin J.E., 1973, *MNRAS*, 163, 163
- Zaritsky D., Kennicutt R.C., Huchra J.P., 1994, *ApJ*, 420, 87
- Zinchenko I.A., Pilyugin L.S., Grebel E.K., Sánchez, S.F., Vílchez J.M., 2016, *MNRAS*, 462, 2715
- Zinchenko I.A., Pilyugin L.S., Sakhিবov F., et al., 2019, *A&A*, 628, A55